EPR OF SUBSTITUTIONAL AND OF CHARGE COMPENSATED Fe^{3+} IN ANATASE (TiO_2) AND ITS TEMPERATURE DEPENDENCE

by

Manfred Horn

A THESIS SUBMITTED IN PARTIAL FULFILMENT OF THE REQUIREMENTS FOR THE DEGREE OF DOCTOR OF PHILOSOPHY

in the Department of Physics

We accept this thesis as conforming to the required standard

THE UNIVERSITY OF BRITISH COLUMBIA

June, 1971

In presenting this thesis in partial fulfilment of the requirements for an advanced degree at the University of British Columbia, I agree that the Library shall make it freely available for reference and study. I further agree that permission for extensive copying of this thesis for scholarly purposes may be granted by the Head of my Department or by his representatives. It is understood that copying or publication of this thesis for financial gain shall not be allowed without my written permission.

Department of Physics

The University of British Columbia
Vancouver 8, Canada

Date Aug 10, 1971

ABSTRACT

Paramagnetic resonances were observed in natural single crystals of anatase between 1 ^{o}K and 1230 ^{o}K and are interpreted as due to regular substitutional Fe^{3+} (I) and to Fe^{3+} combined with an oxygen vacancy at a nearest neighbour site (II). The spin Hamiltonian parameter b_2^{o} of (I) decreases from $+457 \times 10^{-4}$ cm^{-1} at 1 ^{o}K almost linearly to -225×10^{-4} cm^{-1} at 1230 ^{o}K. This unusually strong temperature dependence of b_2^{o} and the observed temperature dependence of the orientation of the magnetic axes of spectrum (II) are both explained by assuming that the positions of the oxygen ions within the unit cell are temperature dependent.

TABLE OF CONTENTS

	Page
Abstract	ii
List of Tables	v
List of Figures	vi
Acknowledgements	x
1. Introduction	1
2. Results of previous investigations on anatase	4
2.1. Crystal structure	4
2.2. Phase transformation to rutile	7
2.3. Other properties of anatase	9
2.4. EPR studies of anatase	10
3. Spin Hamiltonian and crystal field	14
3.1. Spin Hamiltonian for Fe^{3+} in an intermediate crystal field	14
3.2. Zero-field splitting of S-state ions and its temperature dependence	18
4. Samples and experimental technique	22
4.1. Natural crystals of anatase	22
4.2. Synthetic anatase powders	22
4.3. X-band EPR spectrometer	23
4.4. Angular plots of EPR spectra	25
4.5. Variable temperature measurements	30
5. Experimental results	35
5.1. Preliminary observations	35
5.2. EPR spectrum I	38
5.3. Temperature dependence of spectrum I	43
5.4. EPR spectra II	48
5.5. Temperature dependence of spectra II	56

Page

6. Discussion of results 59
6.1. EPR spectrum I: substitutional Fe^{3+} 59
6.2. EPR spectra II: charge compensated Fe^{3+} 65
6.3. Conclusions 69

Bibliography 71

Appendix A. Matrix elements of the Spin Hamiltonian (8) for S = 5/2 and the magnetic field H along one of the coordinate axes 78

Appendix B. Approximate calculation of b_2^0 and b_2^2 of spectrum II 80

Appendix C. Calculation of spin Hamiltonian parameters with a linearized least mean square fit 83

LIST OF TABLES

		Page
Table I.	Previous EPR results with anatase	11
Table II.	Spin Hamiltonian parameters of spectra I and II in anatase at 78 ^{o}K and 300 ^{o}K	40
Table III.	Linewidths of spectrum I in anatase at room temperature	40
Table IV.	Directions of the magnetic axes for spectrum II_A in anatase, expressed in polar coordinates (θ, ϕ). The axes of the other three spectra II are obtained by successive rotations of 90^{o} about the [001] crystal axis	50
Table V.	Matrix for the spin Hamiltonian (8) for S = 5/2 and H // z.	78
Table VI.	Expressions to be inserted in place of b_n^m in Table V for the cases when H is along the x or y axis	79

LIST OF FIGURES

		Page
Fig.1	The positions of the ions in a unit cell of anatase	5
Fig.2	Block diagram of the field locked EPR spectrometer arrangement which will automatically trace the angular dependence of EPR transition fields	27
Fig.3	Experimental arrangement for measuring angular plots or relative angular positions of EPR lines	28
Fig.4	Cross-section of the cavity with the high-temperature heating elements in place	32
Fig.5	EPR spectrum at X-band of a natural anatase crystal with H parallel to [001] at room temperature	36
Fig.6	EPR spectrum at X-band of a natural anatase crystal with H parallel to [100] at room temperature	37

Page

Fig.7 Angular dependence of EPR lines of spectrum I in anatase at X-band with H rotated in three different crystal planes 39

Fig.8 Peak heights of the outer fine structure lines of spectrum I in anatase with H rotated in the (001)-plane, normalized to 1 at H // [110] 42

Fig.9 EPR spectra at X-band of a natural anatase crystal with H parallel to [001] at 449 °C, 495 °C and 754 °C 44

Fig.10 Temperature dependence of EPR lines of spectrum I at X-band of anatase with H parallel to [001] as a function of temperature 45

Fig.11 Temperature dependence of b_2^0 and b_4^0 of spectrum I in anatase 46

Fig.12 EPR spectra of a natural crystal at X-band with H parallel to [110] at 239 °C and 861 °C and with H parallel to [100] at 721 °C 47

Page

Fig.13 Spectra II in the (100)-crystal plane of anatase at room temperature and 9.19 GHz. 23 KGauss was the highest obtainable field. The lower part of the figure shows a spectrum obtained by rotating the crystal in the (100)-plane at a constant field H = 7200 Gauss 49

Fig.14 EPR spectrum at X-band and room temperature of synthetic anatase powder doped with 1 mol-% of Fe 52

Fig.15 Energy levels of a paramagnetic centre II in anatase with H parallel to each of the three magnetic axes. The observed transitions are indicated and numbered as in Fig.13 54

Fig.16 Temperature dependence of the angle $2\varphi'$, as defined in the text. Approximately φ' gives the magnetic axes of the four spectra II, defined in Table IV 58

Fig.17 Lattice sums B_2^0 and $(B_4^0)'$, calculated with a point charge model of anatase as a function of the oxygen parameter u 62

Page

Fig.18 Effective g values at low field for transitions within the two lower Kramer doublets of the ground state of Fe^{3+} (Ref.51) 80

Fig.19 Positions of the EPR transitions within the two lower Kramer doublets of Fe^{3+} for E/D = 0.25 (Ref.52) 82

ACKNOWLEDGEMENTS

I would like to thank Dr. C.F. Schwerdtfeger for his supervision and assistance in the preparation of this thesis. The research of the thesis was supported financially by the National Research Council of Canada through research grants to Dr. C.F. Schwerdtfeger.

In addition, I am grateful to Dr. E. Meagher for his help in the X-ray analysis of anatase and related problems. To Dr. M.H.L. Pryce I am thankful for discussions on theoretical aspects of the interpretation of the observed spectra and the spin Hamiltonian.

Scholarships from the Ford Foundation and the Universidad Nacional de Ingenieria, Lima, Peru, which I got through the kindness of Dr. V. Latorre, are gratefully acknowledged.

Lastly, I must acknowledge the constant encouragement and help I received from my wife Rosario in completing this research.

1. INTRODUCTION

It has long been known that the same chemical compound can crystallize in different forms. This phenomenon is called polymorphism[1].

For many years it has been recognized that the minerals anatase*, brookite and rutile are polymorphic forms of titanium dioxide[2]. More recently, a fourth polymorph of TiO_2, the synthetic high pressure TiO_2II, was produced[3].

Good crystals of the three naturally occuring polymorphs of TiO_2 have been found. Synthetically one can grow single crystals of rutile with the Verneuil method[2] and polycrystalline anatase. The techniques to obtain synthetic single crystals of anatase and brookite, or even polycrystalline brookite, are however still not well developed[4,5]. As a result, most studies on the properties of TiO_2 have been made with rutile. This is particularly true for investigations utilizing Electron Paramagnetic Resonance (EPR) techniques. Whereas numerous EPR studies have been reported on paramagnetic impurities and defects in rutile[6,7], only a few of anatase (discussed in section 2.4.) and none of brookite have been published.

The interest in EPR studies of rutile is based mainly on two facts. First, the basic structural blocks of rutile

---

* In older literature also named octahedrite, in allusion to its common octahedral habit.

are TiO_6 octahedra, the same as in $BaTiO_3$ and other ferroelectrics with perovskite structure. An understanding of the properties of the structurally and chemically simpler rutile can therefore help to explain the ferroelectric phase transitions in perovskites. Second, rutile has very good dielectric properties (high dielectric constant and low loss factor) and the electronic ground state splittings and relaxation times of iron and chromium impurities are appropriate for its use as a maser material[7].

The same arguments should also apply for anatase and brookite where the structural difference from rutile lies mainly in the different stacking of the TiO_6 octahedra. A thorough EPR study of these minerals was therefore thought to be worthwhile.

In addition to this, there exists also an interest in a comparative EPR study of the different polymorphic forms of TiO_2 from a mineralogical point of view. Particular mineralogical problems are: Which factors determine that TiO_2 crystallizes in one case as rutile and in other cases as anatase or brookite? Which impurities are found in the different polymorphs, in which quantities and on which sites within the crystal? Reviews by W. Low[8] and S. Ghose[9] have shown that EPR can help to clarify mineralogical problems of this kind.

In the present thesis the results of an EPR analysis of iron impurities in natural single crystals of anatase are

described and are supplemented with the analysis of synthetic polycrystalline anatase doped with iron. In view of the small number of studies of the properties of anatase and the absence of an up to date compilation of these data, a short summary of previous works on anatase will be given before discussing the results of the present investigation.

The main results of this investigation have been published elsewhere[10].

2. RESULTS OF PREVIOUS INVESTIGATIONS ON ANATASE

2.1. Crystal structure

Anatase has tetragonal symmetry and belongs to the space group $I4_1/amd$ (D_{4h}^{19}) (which includes a centre of symmetry, e.g. halfway between the oxygen ions A and F, as labelled in Fig.1) [11]. In Fig.1 is shown a unit cell. All Ti ions sit on special sites with point symmetry $\bar{4}2m$ (D_{2d}), whereas the positions of the oxygen ions, which have point symmetry mm, is completely determined experimentally by measuring the "oxygen parameter" u, as indicated in Fig.1. D. Cromer and K. Herrington[12] determined u at room temperature, as well as the cell dimensions a and c from X-ray powder data. Their results are

$$\begin{aligned} a &= 3.785 \pm 0.001 \text{ Å} \\ C &= 9.514 \pm 0.006 \text{ Å} \\ u &= 0.413 \pm 0.002 \text{ Å} \end{aligned} \qquad (1)$$

The unit cell as shown in Fig.1 contains four "molecules" of TiO_2. However, some authors refer to a larger unit cell with eight molecules, with the same c as given in (1) but an a which is $\sqrt{2}$ times larger. This unit cell is rotated 45° around the c axis, [001], with respect to the smaller one shown in Fig.1. While defining crystallographic axes one has therefore to be careful which is the underlying choice of the unit cell.

As can be seen from Fig.1 each titanium ion is

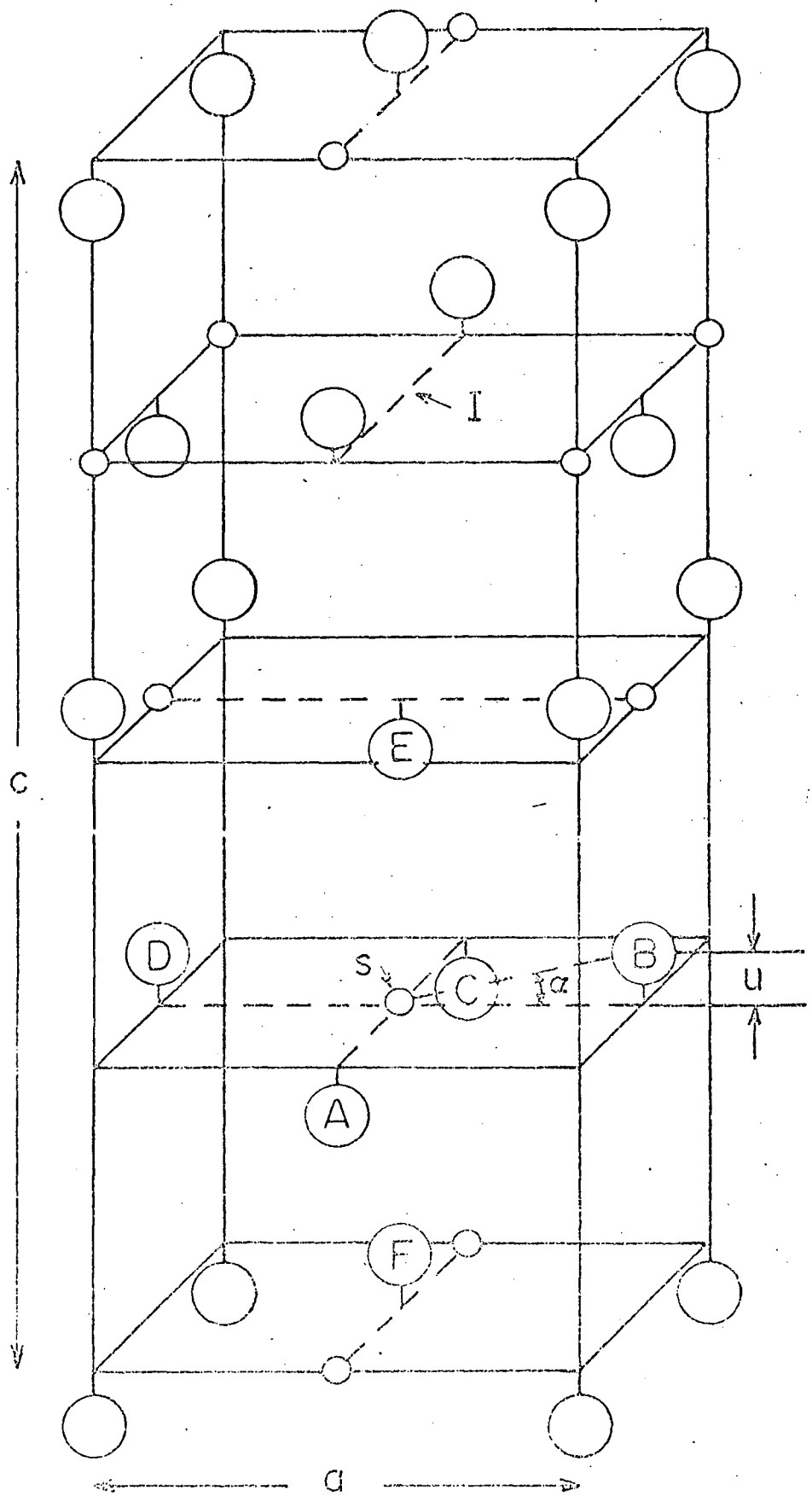

Fig.1 The positions of the ions in a unit cell of anatase

surrounded by six oxygen ions at the corners of a distorted octahedron and every oxygen ion by three titanium ions. Each TiO_6 octahedron shares 4 edges with other TiO_6 octahedra and the shared edges are, in accordance with Paulings rule[13], shortened (thus increasing the distance between neighbouring highly charged Ti^{4+} ions). From the values for a, c and u, as given in (1), one can calculate the nearest neighbour distances to:

4	Ti-O	1.937 Å	SA, SB, SC, SD
2	Ti-O	1.964 Å	SE, SF
4	O-O	2.802 Å	AB, BC, CD, DA
4	O-O	2.446 Å	BE, DE, AF, CF
4	O-O	3.040 Å	AE, CE, DF, BF

(2)

The last column of (2) refers to the identification of individual ions in Fig.1. The titanium ion at S has as nearest neighbours the four oxygen ions at A-D.

Fig.1 shows also that each unit cell contains four interstitial sites, one is marked with I, with the same symmetry elements as the Ti^{4+} site. The only difference from the Ti^{4+} site is that the surrounding oxygen octahedra are longer along the [001] axis with an $I\text{-}O^{2-}$ distance of 2.792 Å.

Another way of viewing the structure of anatase is the following: the oxygen ions, which have an ionic radius of 1.32 Å [14], are approximately in a cubic close packed arrangement with layers parallel to the (112)-crystal planes. All the

tetrahedral voids of this cubic close packed structure are empty and half of the octahedral voids are filled with the small Ti^{4+} ions, with an ionic radius of 0.69 Å [14], which lie in zig-zag lines parallel to [221].

It is interesting to compare one particular feature of this structure with that of rutile. In rutile, where the individual TiO_6 octahedra have an orthorhombic distortion and share only two edges with other octahedra, the distance between neighbouring Ti^{4+} and O^{2-} ions is 1.946 Å and 1.984 Å [12]. These distances are greater than the equivalent ones in anatase and result in a volume for a TiO_6 octahedron of 9.9 $Å^3$, as compared to 9.4 $Å^3$ for anatase. In spite of this, the different stacking results in the density of rutile being 7% higher than that of anatase.

2.2. Phase transformation to rutile

A. Navrotsky and O. Kleppa[15] have shown that anatase is, under all temperature and pressure conditions, thermodynamically metastable. Under heating, anatase transforms irreversible to the stable rutile. Of interest in this connection is the work of W. Beard and W. Foster[16] who found anatase in a quenched melt of TiO_2 and SiO_2, and TiO_2 and B_2O_3 from 1660 °C and above, thus indicating a high temperature formation of anatase, whereas normally in the laboratory anatase is formed by dehydration of precipitated titanium hydroxide at lower temperatures[17].

Several authors have studied the kinetics of the transformation of anatase to rutile[18-21]. The results can be summarized as follows.

The rate of transformation and its activation energy are governed by the surface size and by the nature and amount of impurities which determine the defect structure of anatase, e.g. the concentration of oxygen vacancies or interstitials. Spectroscopically pure anatase powder transforms to rutile after heating above a threshold temperature of 610 °C [19]. The activation energy is 80 kcal/mol, which is mainly the activation energy for the production of the nucleation sites. The rate of transformation is therefore governed by the rate of nucleation. The effect of impurities in general is that oxygen vacancies accelerate, interstitial ions inhibit the transformation[21]. The former are produced by Cu^{2+}, Li^{+}, Na^{+}, Cr^{3+}, Fe^{3+}, which substitute for Ti^{4+}, whereas Ca^{2+}, Sr^{2+}, Zn^{2+}, Cl^{-}, P^{5+}, S^{6+} incorporate as interstitial ions or generate interstitial Ti^{3+}. According to the impurities present, the threshold temperature for the transformation can vary from 400 °C to 1200 °C.

Dachille, Simons and Roy[22] determined the influence of pressure on the transformation, establishing apparent stability ranges of anatase, brookite, rutile and TiO_2II in a P,T diagram.

Shanon and Pask[23] proposed a mechanism for the transformation of anatase to rutile: starting with the experimental

evidence that rutile crystals formed in transformed single crystals of anatase have particular preferred orientations, they assumed retention of the {112} pseudo close packed planes of oxygen in anatase as the {100} pseudo close packed planes in rutile, and rearrangement of the titanium and oxygen ions within these planes.

2.3. Other properties of anatase

Other physical properties of anatase that have been investigated are the basic mechanical, thermal and optical ones. If not otherwise indicated, the following values are taken from references 17 and 24, where also more, and usually older, data can be found. Values in parentheses refer to rutile.

Anatase crystals show perfect cleavage parallel to (001) and {011}. The density is 3.87 - 3.95 gm/cm^3 (4.21 - 4.25) and the hardness is 5.5 - 6.0 (7.0 - 7.5).

Rao[25] measured with an X-ray high temperature powder camera the lattice constants a and c up to 712 ^oC. Over this temperature range he obtained a continuous increase of c and a, with c increasing more rapidly than a. At room temperature he obtained the thermal expansion coefficients $\alpha_{\parallel} = 7.8 \times 10^{-6}\ ^oC^{-1}$, $\alpha_{\perp} = 3.8 \times 10^{-6}\ ^oC^{-1}$ and at 712 ^oC $\alpha_{\parallel} = 19.5 \times 10^{-6}\ ^oC^{-1}$ and $\alpha_{\perp} = 9.5 \times 10^{-6}\ ^oC^{-1}$. Over a temperature range of 500 ^oC c increased 0.6% and a, 0.3%. Schroeder[26] measured optically the change of the quotient $\alpha_{\parallel}/\alpha_{\perp}$ by measuring the angle of a

prism cut conveniently out of a yellow anatase crystal from Binnental, Switzerland. $\alpha_{\parallel} / \alpha_{\perp}$ increased linearly up to 642 $\pm$ 3 ^{o}C and beyond this temperature again linearly, but with a different slope, up to 900 ^{o}C where anatase started to transform into rutile. This behaviour below 900 ^{o}C was completely reversible. Schroeder concluded that at 642 ^{o}C anatase undergoes a reversible phase change to a high temperature structure, named α - anatase, with probably also tetragonal symmetry.

The specific heat at room temperature is 13.22 cal/mol^{o}C (13.16).

Synthetic powders of anatase are white. Natural crystals have various colors, from brown, yellow, greenish, passing into blue and black but rarely colorless. The optical constants vary markedly with wavelength and temperature. The indices of refraction n_o and n_e decrease continuously with temperature[26] up to 900 ^{o}C, with n_o decreasing faster than n_e, so that the birefrigence decreases also. At room temperature $n_o^{5893\text{Å}} = 2.56(2.61)$, $n_e^{5893\text{Å}} = 2.49(2.90)$.

Anatase is an insulator at room temperature. The static dielectric constant of the synthetic powder is $\varepsilon = 48(114)$ [27].

2.4. EPR studies of anatase

The previous EPR results obtained with anatase are summarized in Table I. The parameters quoted there have the

TABLE I. Previous EPR Results with Anatase

Values in parentheses refer to rutile[7]

Paramagn. species	Location	T °K	Freq. band	Seff	$g_{\parallel}$ or g_x g_y	$g_{\perp}$ or g_z	D $10^{-4}cm^{-1}$	Remarks Energies in $10^{-4}cm^{-1}$	Ref.
Fe^{3+}	Substit. for Ti^{4+}	300 (4.2-300)	X	5/2	2.009 (2.00)	2.002	$\pm$ 309 (+6780)	natural single crystal F = $\pm$ 308(+230) a = $\pm$ 99(-280)(E = + 690)	28
Cr^{3+}	Substit. for Ti^{4+}	300 (4.2-300)	X	3/2	1.973 (1.97)		373 (-6800)	Synthetic powder A^{53Cr} = 17(16.7)(E=-2270)	29
Ti^{3+}	Substit. for Ti^{4+}	83 - 173 (4.2)	X.Q	1/2	1.990 (1.975)	1.959 (1.953)		Synthetic powder, doped with Sb^{5+}	30, 31
	Interstit.			1/2	1.987 (1.972)	1.966 (1.940)		($A^{47,49Ti}$ = 1.9 - 2.2)	
$(TiO)^{3+}$	near surface, in the bulk	300	X	1/2	2.023 2.052	1.983		Synthetic powder, heated under oxygen atm.at 450 °C $A^{47,49Ti}$ = 1.3	32
O_2^-	on surface	83-300	X	1/2	three g values between 2.023 and 1.98			Synthetic powder, heat and oxygen treated. Also other lines are observed, which are assoc.with Ti^{3+} and F-center on surface	33
O_2^+	on surface	1.6-300	X,Q	1/2	1.977 1.999	2.022		Synthetic powder, heat and oxygen treated.	34

usual meaning (for their explicit definition see chapter 3 of this thesis).

The only published single crystal study was made by D. Gainon and R. Lacroix[28]. They reported a single magnetic spectrum in a natural crystal of anatase, which they associated with Fe^{3+} impurities substituting for Ti^{4+}. Their two main conclusions were that:

(i) "D is much smaller than for the Fe^{3+} ion in the rutile form of TiO_2".

(ii) "The ratio D/F is very near unity, while it is at least more than ten times larger in all the other cases we know". (Literal quotations). As Gainon and Lacroix made only room temperature measurements they could determine only the relative signs of the spin Hamiltonian parameters, however, they conclude that the upper sign, as given in Table I, "is more likely correct, because for all experiments yet known, a has a positive sign".

T. Barry[28] analysed Cr^{3+} doped anatase powder at room temperature. He observed five powder lines which he could describe by the spin Hamiltonian parameters given in Table I. The crystal field term D (only the absolute value was measured) is similar to that for Fe^{3+}, as established by Gainon and Lacroix, and the spectroscopic splitting factor is typical for Cr^{3+} in weak octahedral crystal field. The hyperfine splitting constant A for ^{53}Cr is the same as in rutile.

In addition to these two studies on paramagnetic impurities in anatase some EPR analyses on defects in anatase have been reported. M. Che et al.[30] report two EPR spectra in Sb^{5+} doped anatase powder, which they described as due to Ti^{3+} ions in different crystal locations with axial symmetry, probably substitutional and interstitial. C. Hauser and P. Cornaz[32] report two EPR powder spectra with orthorhombic symmetry of heat treated anatase powder and interpret them as due to $(TiO)^{3+}$ complexes near the surface.

The last two studies, as given in Table I, describe EPR lines which are associated with O_2^- and O_2^+ radicals attached to the surface of anatase powder.

3. SPIN HAMILTONIAN AND CRYSTAL FIELD

In this chapter the spin Hamiltonian and the theoretical interpretation of its parameters will be discussed in as much as it is relevant to the observed EPR spectra of Fe^{3+} in anatase.

3.1. Spin Hamiltonian for Fe^{3+} in an intermediate crystal field

In most cases a crystal field is not strong enough to break down the LS-coupling of the free ions of the 3d-transition elements, but is stronger than the spin-orbit coupling. As a result, the total angular momentum J loses its meaning but L (orbital angular momentum) and S (spin angular momentum) remain "good quantum numbers". This is called the intermediate crystal or ligand field case.

The electronic configuration of the ion Fe^{3+} is d^5 and the free ion electronic ground state is $^6S_{5/2}$. In an intermediate crystal field the ground state is an orbital singlet. Owing to the crystal field and/or an external magnetic field H its 6-fold spin-degeneracy is lifted. Neglecting a possible interaction with surrounding nuclear spins or the nuclear spin of the 2% abundant ^{57}Fe, the fine structure of the ground state is conveniently described by the spin Hamiltonian (Abragam and Bleaney[35]; this is the main reference source for the present chapter)

$$\mathcal{H} = ß\,\vec{H}\,.\,\tilde{g}\,.\,\vec{S} + \frac{1}{3}\sum_{m=-2}^{2} b_2^m\, O_2^m + \frac{1}{60}\sum_{m=-4}^{4} b_4^m\, O_4^m \qquad (3)$$

The first term in (3) represents the usual magnetic field dependence, ß is the Bohr magneton and $\tilde{g}$ the spectroscopic splitting tensor. Experimentally (and also theoretically) $\tilde{g}$ is found to be nearly isotropic and to differ at most a fraction of 1% for Fe^{3+} in a variety of host crystals.

The b_n^m in (3) can be considered as experimental constants and the O_n^m are operator equivalents, formed from polynomials of the spin operator $\vec{S}$, so that they have the same transformation properties as the corresponding spherical harmonics Y_n^m. In the present case the important O_n^m are[36]

$$O_2^0 = 3S_z^2 - S(S+1)\;;\quad O_2^2 = 1/2\,(S_+^2 + S_-^2) = S_x^2 - S_y^2.$$

$$O_4^0 = 35S_z^4 - 30S(S+1)S_z^2 + 25S_z^2 - 6S(S+1) + 3S^2(S+1)^2$$

$$O_4^4 = 1/2\,(S_+^4 + S_-^4) \qquad (4)$$

$$O_4^2 = 1/4\left\{\left[7S_z^2 - S(S+1) - 5\right](S_+^2 + S_-^2) + (S_+^2 + S_-^2)\left[7S_z^2 - S(S+1) - 5\right]\right\}$$

Appropriate basis functions for (3) are the eigenfunctions $|M\rangle$, $M = -5/2, -3/2, \ldots, +5/2$ of the operator S_z. The operators O_n^m connect then a state $|M_1\rangle$ only with $|M_2\rangle$, where $|M_1 - M_2| = m$.

Spin operators of higher degree than five need not to be included in (3) because all of their matrix elements are zero within the manifold of S = 5/2. Spin operators of odd degree have also zero matrix elements, because they do not fulfill time reversal invariance (the components of $\vec{S}$ are odd operators under time reversal).

The constants b_n^m are related to D, E, a and F used in many EPR studies by the relations

$$b_2^0 = D \qquad b_4^0 = a/2 + F/3$$
$$b_2^2 = 3E \qquad b_4^4 = 5a/2 \tag{5}$$

Using the known transformation properties of Y_n^m under rotation of the coordinate system, one can evaluate the transformation properties of the b_n^m under these rotations. Explicit formulae are given by V. Vinokurov et al.[37,38] and J. Thyer et al.[39].

The number of necessary coefficients b_n^m can be reduced by choosing a special coordinate system and is further reduced according to the symmetry of the crystal field. In particular, a cubic crystal field

$$V_c \propto (x^4 + y^4 + z^4 - 3/5\ r^4) \tag{6}$$

gives rise to an operator equivalent $O_4^0 + 5\,O_4^4$, so that it can be described by a single parameter $a = 2/5\,b_4^4 = 2\,b_4^0$ provided one chooses the three fourfold axes as the reference system. All other b_n^m are then zero. If one uses, however, a fourfold axis as z-axis and the two perpendicular twofold axes as x- and y-axes, one obtains b_4^4, and therefore a, of opposite sign and an additional apparent axial distortion $F = -3a$. It is now apparent that Gainon and Lacroix[28] must have used this latter coordinate system to describe the EPR spectrum of substitutional Fe^{3+} in anatase, resulting in an unusual negative value for a and a very large F (Gainon and Lacroix established only that a has an opposite sign to D, but D is positive, as will be discussed below). *

The observed EPR spectra of Fe^{3+} in anatase indicate that the Fe^{3+} ions are located in two different crystal fields. The first one is mainly cubic with an additional distortion along a tetragonal axis. The resulting axial crystal field is represented by the spin Hamiltonian

$$\mathcal{H} = g_{\parallel}\ \beta\ H_z\ S_z + \frac{1}{2}\,g_{\perp}\ \beta\ H_{\perp}\ (S_+ + S_-)$$
$$+ \frac{1}{3}\,b_2^0\ O_2^0 + \frac{1}{60}\,b_4^0\ O_4^0 + \frac{1}{60}\,b_4^4\ O_4^4 \qquad (7)$$

The only symmetry of the crystal field at the second sites is given by a reflection plane through the paramagnetic

---

* A reinterpretation of the results of Gainon and Lacroix was given by M. Horn and C.F. Schwerdtfeger[40].

ions. The appropriate coordinate system is then given by the x-and z-axes in this plane and the y-axis perpendicular to the reflection plane (ref.35, p.667). This makes $b_n^m = 0$ for $m<0$. The directions of the two axes in the plane can be chosen so that $b_2^1 = 0$. This implies the choice of the principal axes of the second order tensor b_2^m as coordinate axes and is specially appropriate if the terms b_2^m are much larger than the fourth order terms b_4^m, because then the experimentally determined "magnetic axes", defined by extreme positions of the EPR spectral lines, coincide with the coordinate axes. As will be discussed in chapter 5, only b_4^m with m even are considered in the description of the observed EPR spectra of anatase, so that the resulting spin Hamiltonian has the form

$$\mathcal{H} = \beta \vec{H} \cdot \tilde{g} \cdot \vec{S} + \frac{1}{3} b_2^0 O_2^0 + \frac{1}{3} b_2^2 O_2^2 + \frac{1}{60} \sum_{m=0,2,4} b_4^m O_4^m \quad (8)$$

By eventual permutation of the axes one can additionally limit the value of b_2^2/b_2^0 to the range $0 \leq b_2^2/b_2^0 \leq 1$ (ref.41).

3.2. Zero-field splitting of S-state ions and its temperature dependence

If the ground state of Fe^{3+} in an intermediate crystal field were a pure $^6S_{5/2}$, its sixfold spin degeneracy would not be lifted and all b_n^m of the spin Hamiltonian (3) would be zero. Experimentally however, one observes a fine

structure of the ground state and several mechanisms have been proposed to explain it. (An up to date list of references is given by A. Serway[42]). Spin-spin and spin-orbit interaction produce second or higher order terms coupling the ground state through higher orbital states to the crystal field. The results for b_2^0 (=D) can be summarized in

$$b_2^0 = b_o + c_1 B_2^0 + c_2 (B_4^0)' + c_3 (B_2^0)^2 \qquad (9)$$

The B_n^m are coefficients of a development of the electric crystal field V at the paramagnetic ion site in spherical harmonics Y_n^m

$$V = \sum_{n,m} \left(\frac{4\pi}{2n+1}\right)^{1/2} B_n^m r^n Y_n^m \qquad (10)$$

$(B_4^0)'$ is the remaining part of B_4^0 after substracting the part corresponding to a perfect cubic crystal field. b_o accounts for covalent bonding and overlap of the electrons of the paramagnetic ion with the surrounding ligands and the c_i are constants determined by properties of the paramagnetic ion, such as spin-orbit coupling and orbital level splitting in a cubic crystal field. R. Sharma, T. Das and R. Orbach[43] have calculated b_2^0 for Mn^{2+} in octahedral coordination of ZnF_2. They find

$$b_2^0 = -0.07 B_2^0 + 0.36 (B_2^0)^2 + 4.34 (B_4^0)' \qquad (11)$$

if b_2^0 is measured in cm^{-1} and B_n^m in $e^2/2a_o^{n+1}$; e is the elementary charge, a_o, the atomic unit of length.

In some cases[43-45], even the use of a point charge model to calculate B_2^0 and $(B_4^0)'$, while neglecting b_0, has resulted in a calculated value of b_2^0 in reasonable agreement with experiment. A point charge model calculation yields[43]

$$B_2^0 = \sum_j q_j \, (3 \cos^2\theta_j - 1) \, / \, R_j^3 \tag{12}$$

$$(B_4^0)' = \sum_j q_j \left\{ \frac{1}{4} \, (35 \cos^4 \theta_j - 30 \cos^2 \theta_j + 3) - \frac{7}{4} \sin^4 \theta_j \cos 4 \phi_j \right\} / \, R_j^5 \tag{13}$$

where the external point charges $q_j |e|$ are situated at (R_j, θ_j, ϕ_j) with respect to an origin taken at the site of the paramagnetic ion.

The above briefly outlined theory explains also to some extent the temperature dependence of the zero-field splitting of S-state ions, because with changing temperature the interionic distances and therefore the components B_n^m of the crystal field will change. Thus R. Sharma[45] qualitatively explained the temperature dependence of D for Mn^{2+} in $CdCl_2$, by calculating B_2^0 and $(B_4^0)'$ with a point charge model of this crystal for different temperatures, using the known thermal expansion of $CdCl_2$.

W. Walsh et al.[46] distinguish between this "implicit" temperature dependence caused by thermal expansion and an "explicit" temperature dependence of the spin Hamiltonian parameters caused by lattice vibrations.

Formally, these implicit and explicit effects can always be separated for any variable which is completely specified by the temperature T and the volume V of the crystal, e.g. for D one can write

$$\left(\frac{\partial D}{\partial T}\right)_P = \left(\frac{\partial D}{\partial T}\right)_V - \frac{\beta}{\kappa}\left(\frac{\partial D}{\partial P}\right)_T \qquad (14)$$

where the first term on the right-hand side is the explicit contribution to D(T) and the second term on the right-hand side is the implicit term. $\beta = \frac{1}{V}\left(\frac{\partial V}{\partial T}\right)_P$ is the thermal volume expansion coefficient and $\kappa = -\frac{1}{V}\left(\frac{\partial V}{\partial P}\right)_T$, the compressibility. The implicit temperature dependence of D may therefore be evaluated if β, κ and the isothermal pressure dependence of D are known. On the basis of a simple "effective point charge model" W. Walsh et al.[46] calculate that the implicit temperature dependence of D and a should depend on the interionic distance r as

$$D \propto r^{7} \quad ; \quad a \propto r^{-21} \qquad (15)$$

where an isotropic thermal expansion is supposed.

4. SAMPLES AND EXPERIMENTAL TECHNIQUE

4.1. Natural crystals of anatase

The five natural crystals of anatase studied in this work originated in Tavetch, Graubünden, Switzerland and Binntal, Wallis, Switzerland. They were kindly supplied by A. Harnik of the Crystallographic Institute of ETH, Zürich, and E. Meagher of the Geology Department of U.B.C., Vancouver.

Typical diameters of the crystals were 1-3 mm. The two Tavetch crystals had pyramidal habit, opaque gray color and their EPR spectra, although qualitatively similar to those of the Binntal crystals, showed broad and poorly resolved lines. The three crystals from Binntal were yellow and transparent. They possessed different habits but always had clear recognizable {110}-planes, which helped to orientate them. One crystal was split in three parts, using the (001)-cleavage planes. The orientation of the crystal axes was checked with back-reflection Laue X-ray photographs.

All the Binntal crystals showed the same EPR spectra and the single crystal results reported here were obtained with them.

4.2. Synthetic anatase powders

The single crystal studies were supplemented with synthetic powder studies. The powders were prepared by

hydrolysis of $TiCl_4$ with NH_4OH (ref.17, p.229). The precipitated TiO_2 powders were crystallized by heating for 24 hours at 400 °C in open porcelan vessels. The powders could be doped by adding 1 mol-% or 0.01 mol-% of aqueous solutions of $FeCl_3$ or $MnCl_2$ to the initial $TiCl_4$. Debye-Scherrer X-ray analysis showed for all powders only anatase lines.

4.3. X-band EPR spectrometer

All EPR spectra were taken at X-band. The X-band EPR spectrometer was of conventional balanced bridge design. As the analysed anatase crystals showed strong EPR signals, no special attention had to be given to operate the EPR spectrometer with maximum sensitivity.

The microwave bridge was formed by a magic T. A reflex-Klystron (Varian V-153/6315; max. output 70 mW), a one-way ferrite isolator and a flap-attenuator were connected to the input arm, a crystal detector (Microwave 1N 23B) to the output. One side arm ended in a TE_{102} resonance cavity (mostly used Varian multi-purpose cavity V-4531), coupled through an adjustable iris. The other reference arm contained a slide screw tuner and a matched load. The crystal diode was biased (100-300 μA) by adjusting either the slide screw tuner or the coupling of the resonance cavity.

The Klystron was frequency locked to the resonance

cavity by modulating the Klystron reflector voltage with 10 kHz and using the corresponding phase sensitive detected output from the crystal detector as an error feedback signal.

The magnetic field was modulated with 100 kHz through small modulation coils attached directly to the resonance cavity. The modulation amplitude used was 0.2-12 Gauss according to the line width of the analysed EPR transition. The pre-amplified output from the crystal detector was phase-sensitive detected at 100 kHz (PAR Lock-in amplifier, model 121). The output of the Lock-in was usually connected directly to a strip chart recorder. In this way one obtained a recording of the first derivative of the EPR absorption lines.

The frequency of the microwaves was measured with a digital frequency meter. (Hewlett-Packard Frequency Converter 5255A and Electronic Counter 5245L).

For most experiments a 9.5" magnet (Magnion) was used with a rotating coil field sensor (Magnion FFC-4 power supply). The maximum obtainable field was 23 kG. The direct reading field sensor dials were calibrated against a NMR-gaussmeter. The permanent magnetic field was always perpendicular to the microwave magnetic field at the sample in the cavity.

4.4. Angular plots of EPR spectra

In order to identify and to analyse the paramagnetic centres in a single crystal one has to measure the EPR transition fields H_t as a function of the orientation of the crystal in the static magnetic field H. Usually one records an EPR spectrum for a given orientation as a function of the field strength H, then rotates either the sample or the magnet through a certain angle in a particular crystal plane, records a new spectrum and so on. To obtain complete graphs of H_t versus angle Θ one requires many spectra implying a great amount of time and energy. This is particularly true if the EPR lines cross one another and if their intensities are strongly angular dependent.

Initially, this method also was applied in the present work to analyse the EPR spectra of the anatase crystals. Later, however, a new technique was used. * It was found that one can obtain these graphs more easily by locking the magnetic field to a particular EPR line and then rotating the crystal slowly with a small motor. In this way one can record directly on an X-Y plotter the desired graphs by supplying to the Y-input a voltage proportional to the instantaneous magnetic field H_t, deduced from a field sensor, and to the X-input of the plotter a voltage indicating the orientation of the sample.

---

* A description of this technique was given by M. Horn and C.F. Schwerdtfeger[47].

Fig.2 gives the block diagramme of this method. Essentially it is the conventional EPR spectrometer as described in the previous section 4.3. But whereas usually the EPR signal output of the Lock-in amplifier goes directly to a recorder, it is now used as an error signal for the control unit of the magnet power supply. This technique is the same as that used to regulate the magnetic field with an NMR sensor[48]. As in every feedback technique one has to ensure that the error signal has the correct polarity. The gain and time constant of the Lock-in amplifier have to be adjusted to give sufficient output voltage to drive the control unit of the magnet power supply but to avoid oscillations (overshooting) of the magnetic field. However, these adjustments are not critical.

In order to monitor the angular position of the specimen, the crystal was mounted directly on the elongated shaft of a 10 turn rear-shaft type Helipot potentiometer (Fig.3), which was connected across a battery as shown in Fig.2. The upper limit of angular resolution obtained in this way was ca. 0.3°, this corresponded to the jumps of the movable contact of the potentiometer from one wire turn to the next. On the other end of the Helipot shaft was mounted a small DC motor with a gearbox allowing rotations in both directions with 0.1 - 4 RPH.

To search for an EPR line, one can either sweep the magnetic field for a particular crystal orientation or rotate

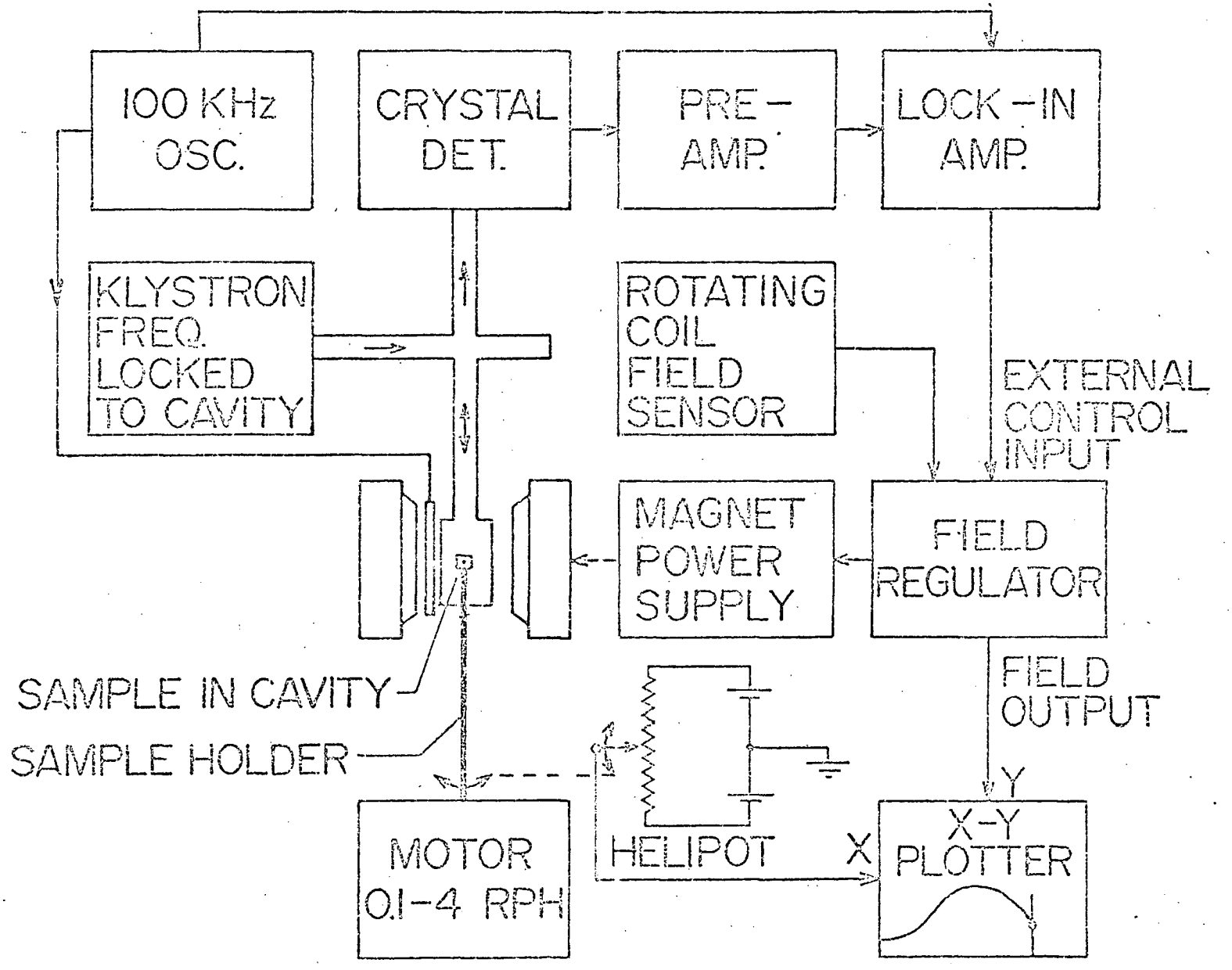

Fig.2 Block diagram of the field locked EPR spectrometer arrangement which will automatically trace the angular dependence of EPR transition fields

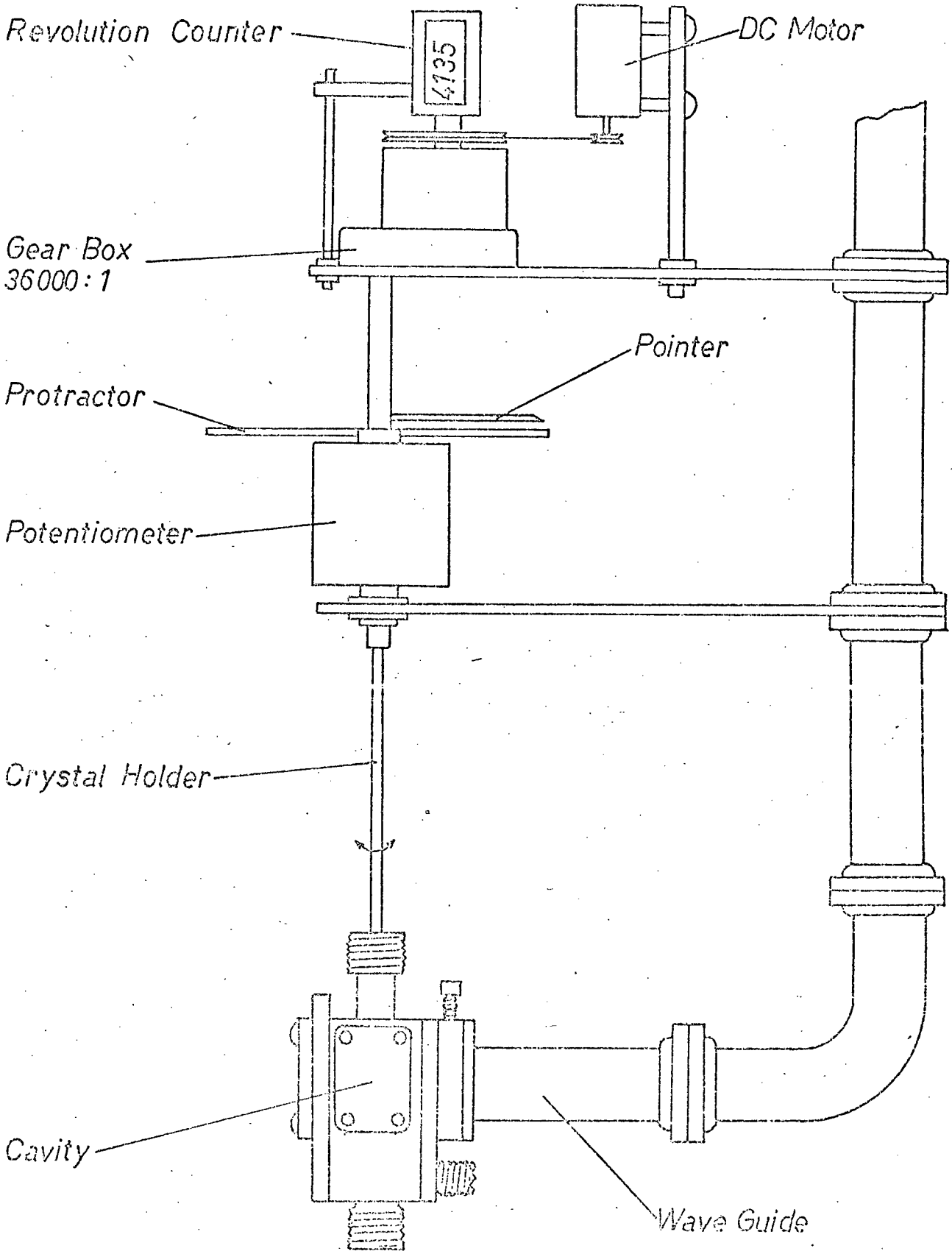

Fig.3 Experimental arrangement for measuring angular plots or relative angular positions of EPR lines

the crystal at a particular fixed magnetic field. If one finds an EPR line in the latter case the magnetic field will automatically lock in on this line and follow it as the crystal is further rotated. If two EPR lines cross, it can happen that the system does not follow the original line. This is immediately recognized by a sudden change in the slope of the curve. To trace the continuation of the original line, one must unlock the field and sweep it to an approximate good position in the H,θ plane and lock in again. The Magnion FFC-4 magnet power supply could follow an external control signal with a maximum change of the magnetic field of 1 kGauss/15 sec, thus limiting the velocity of crystal rotation if the EPR field H_t changes rapidly with angle.

A modification of the above described technique was used to measure accurately relative angular positions of EPR lines. For this purpose, the magnetic field was set to a constant value and the EPR signal output of the Lock-in amplifier was registered on a strip chart recorder while rotating slowly the crystal with the motor. With a revolution counter connected to the input of the gearbox (see Fig.3) the rotation angle could be measured: 1 turn corresponded to 0.01 degree of rotation of the crystal. By selecting appropriate EPR lines the angle between the magnetic axes of different paramagnetic centres could be measured in this way to an accuracy of $\pm$ 0.01 degree.

4.5. Variable temperature measurements

In the early stages of the present work it was recognized that the EPR spectra of the anatase crystals are very temperature dependent. As the analysed temperature range was increased different methods were tried to achieve these temperatures.

Initially, the temperature of the sample was established by a temperature controlled N_2-gas flow. For this purpose a quartz dewar was passed through the sample holes of the cavity. The sample was fixed with refractory cement (Saureisen No.29 Zirconium Base Cement) to a small brass rod (heat sink) which itself was attached to a thin walled stainless steel tube. The sample was inserted from the top into the dewar and could be rotated about the vertical axis. The temperature was measured with a calibrated Chromel-Alumel thermocouple fixed to the brass rod. The lower part of the dewar, outside the microwave cavity, contained a Kanthal wire heater and another thermocouple as monitor. Through a lower hole of the dewar N_2-gas (precooled for temperatures between -190 ^{o}C and room temperature) was introduced. This method is similar to that applied by Varian with its variable temperature accessory V-4557, which permits sample temperatures between -190 ^{o}C and +300 ^{o}C. Using the difference between the voltage of the monitor thermocouple and a standard voltage source as an error feedback signal for the power supply of the heater, the temperature of the sample

could be controlled very accurately. But, this method imposed an upper limit on the sample temperature of approximately 600 °C. The large spacial separation between heater and sample (approx. 7 cm) caused a large temperature gradient between them. In addition, it was difficult to expose the heating wire uniformly to the N_2-gas flow, so that the temperature of some part of the heating wire regularly exceeded the melting point while trying to increase the sample temperature above 600 °C.

Later on a design was used which is a modification of that used by D. Giardino and L. Petrakis[49], who themselves modified a design proposed by L. Singer et al.[50]. The main difference of the new design, shown in Fig.4, is that it permits the use of a Varian standard cavity.

The resistive heating element consists of two strips of platinum about 1 mm wide and bonded to opposite sides of a 6 mm o.d. thin walled quartz tube. The lengths of the platinum strips were about 24 mm, matching the cavity height. The ends of the tube were completely coated with platinum. To obtain these bonded strips, platinum paste (Platinum Paste No.6082, manufactured by the Hanovia Liquid Gold Division of Engelhard Industries Inc.) was applied with a fine brush and fired in a furnace at about 700 °C. Several platinum layers were applied in order to obtain a room temperature resistance of the heater of about 2 ohms.

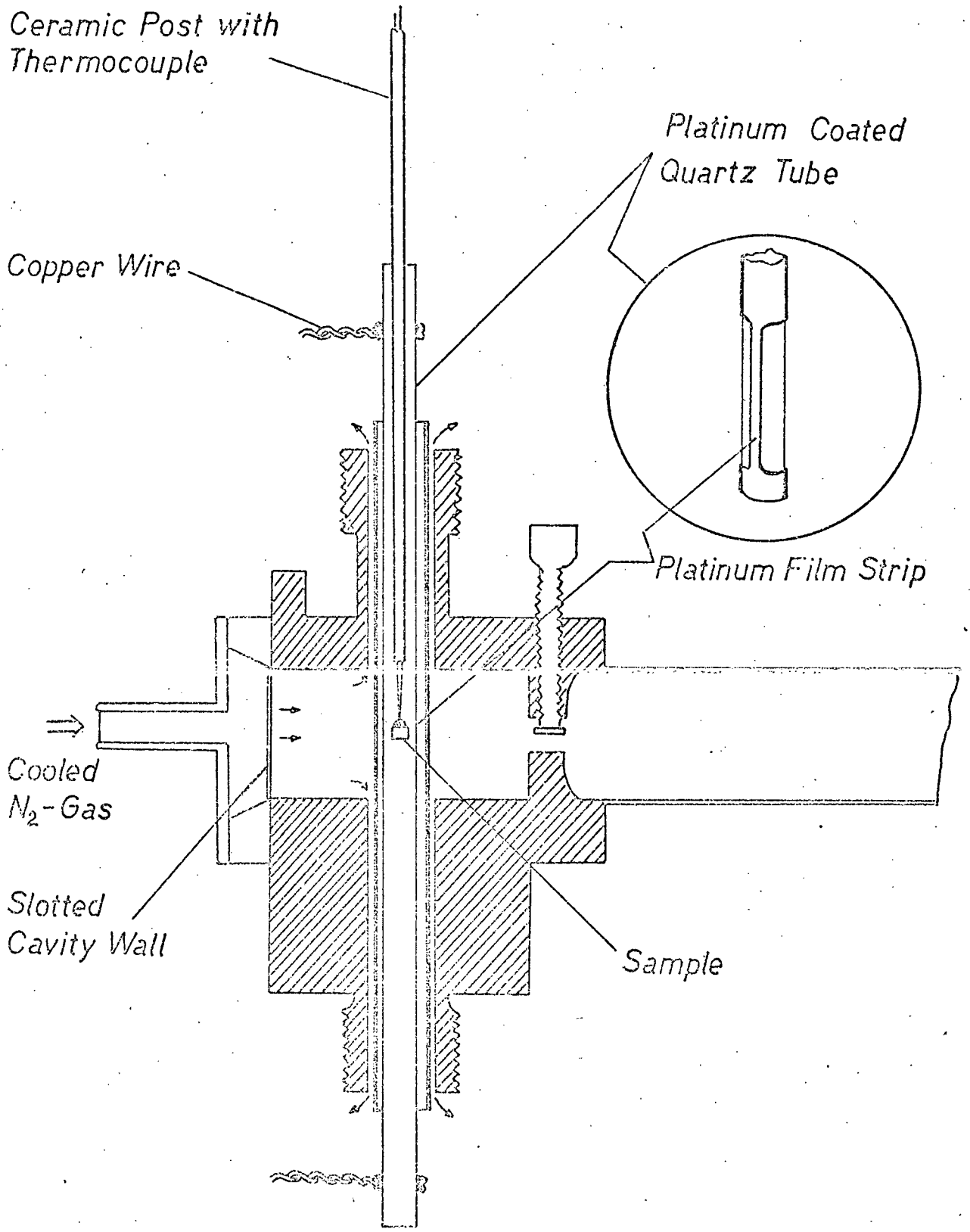

Fig.4 Cross-section of the cavity with the high-temperature heating elements in place

This heater tube was placed coaxially in a 10 mm o.d. quartz tube with 1 mm wall thickness. The two tubes were separated with asbestos between them in the upper and lower parts where the heater tube was completely coated with platinum. Using small teflon spacers (not shown in Fig.4) the combined quartz tubes were then placed in the cavity through the 11.4 mm i.d. sample holes, so that the heater strips coincided with the cavity. Copper wires were bonded near the ends of the heater tube and connected to a regulated DC-power supply (Kepco PR-38-15M). Cooled N_2-gas was introduced in the cavity through the slotted cavity wall. This gas escaped through the small gaps between the 10 mm quartz tube and the inner walls of the sample holes of the cavity.

The sample was glued with a refractory cement directly to a Chromel-Alumel thermocouple passing through a ceramic rod.

This design proved to be trouble free at operation temperatures of up to 1000 ^{o}C. With a moderate flow of cooled N_2-gas the outer cavity walls remained below room temperature. In order to obtain 900 ^{o}C at the sample, an electric power input of about 100 W was needed.

To determine the absolute signs of the spin Hamiltonian parameters of the analysed Fe^{3+} impurities in anatase, EPR measurements at 1 ^{o}K and 4.2 ^{o}K were made. For this purpose a gold-plated brass cavity, operating in TE_{102} mode, was

submerged in liquid helium. The frequency of the field modulation was 400 Hz in these measurements (modulation coils attached to the magnet poles).

5. EXPERIMENTAL RESULTS

5.1. Preliminary observations

Since anatase has tetragonal symmetry one would expect that its EPR spectra would also show this symmetry. This was experimentally verified. The overall EPR spectra of the analysed anatase crystals were the same with the direction of the magnetic field H, expressed in polar coordinates, along (θ, ϕ) and along $(\theta, \pm\phi + n\pi/2)$, where n is an integer.

The EPR spectra at 9.36 GHz and room temperature are shown in Fig.5 with H parallel to the crystallographic [001]-axis and in Fig.6 with H parallel to [100] (in the latter case more lines exist at higher magnetic field).

As a result of the study of the angular dependence of these EPR transitions, one could separate them into two groups, which will be called spectra I and II and which will be discussed separately.

Some weaker EPR lines were observed. However, their intensities and the fact that they overlapped with other lines did not permit even a qualitative interpretation. One of these lines is identified with a question-mark in Fig.6.

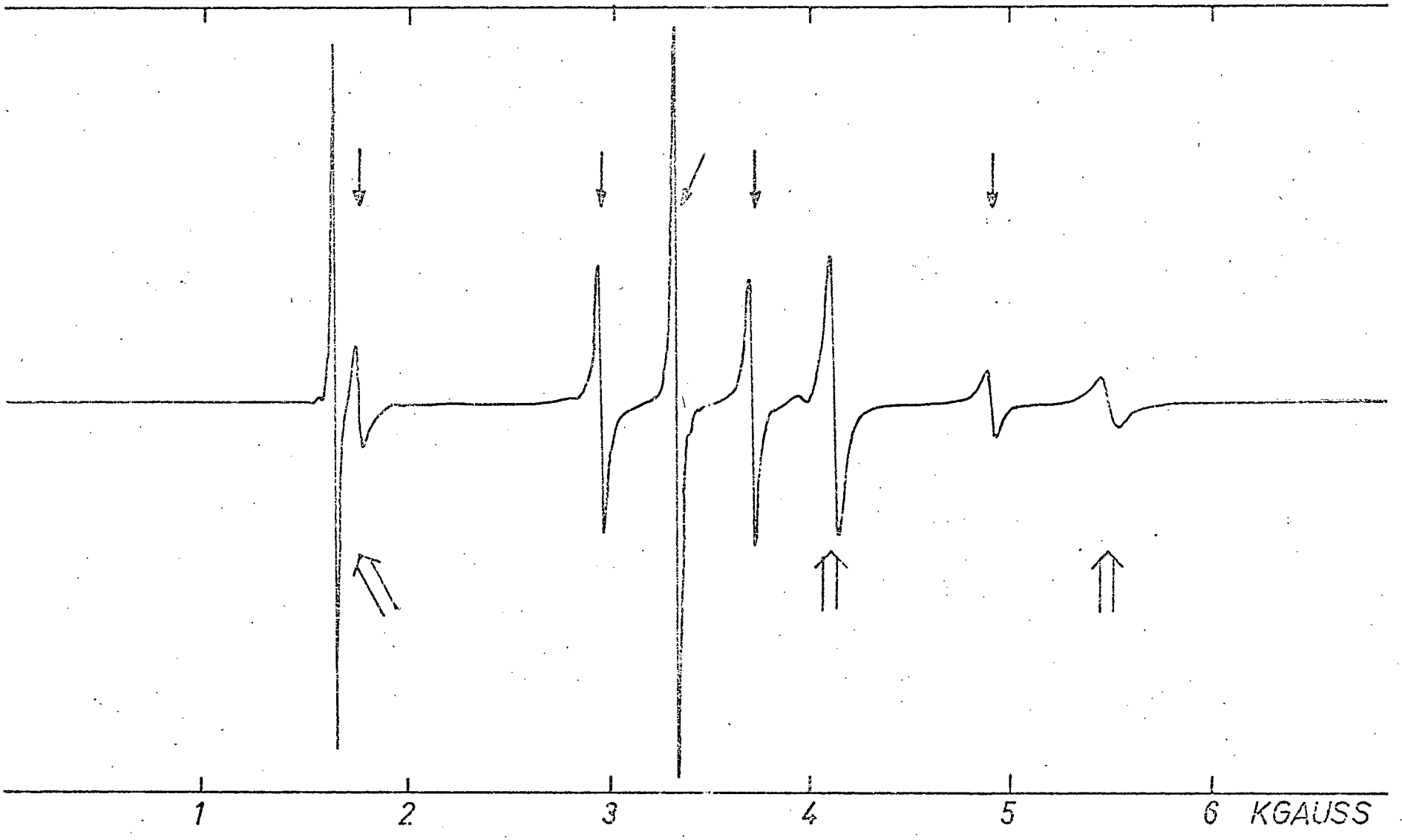

Fig.5 EPR spectrum at X-band of a natural anatase crystal with H parallel to [001] at room temperature

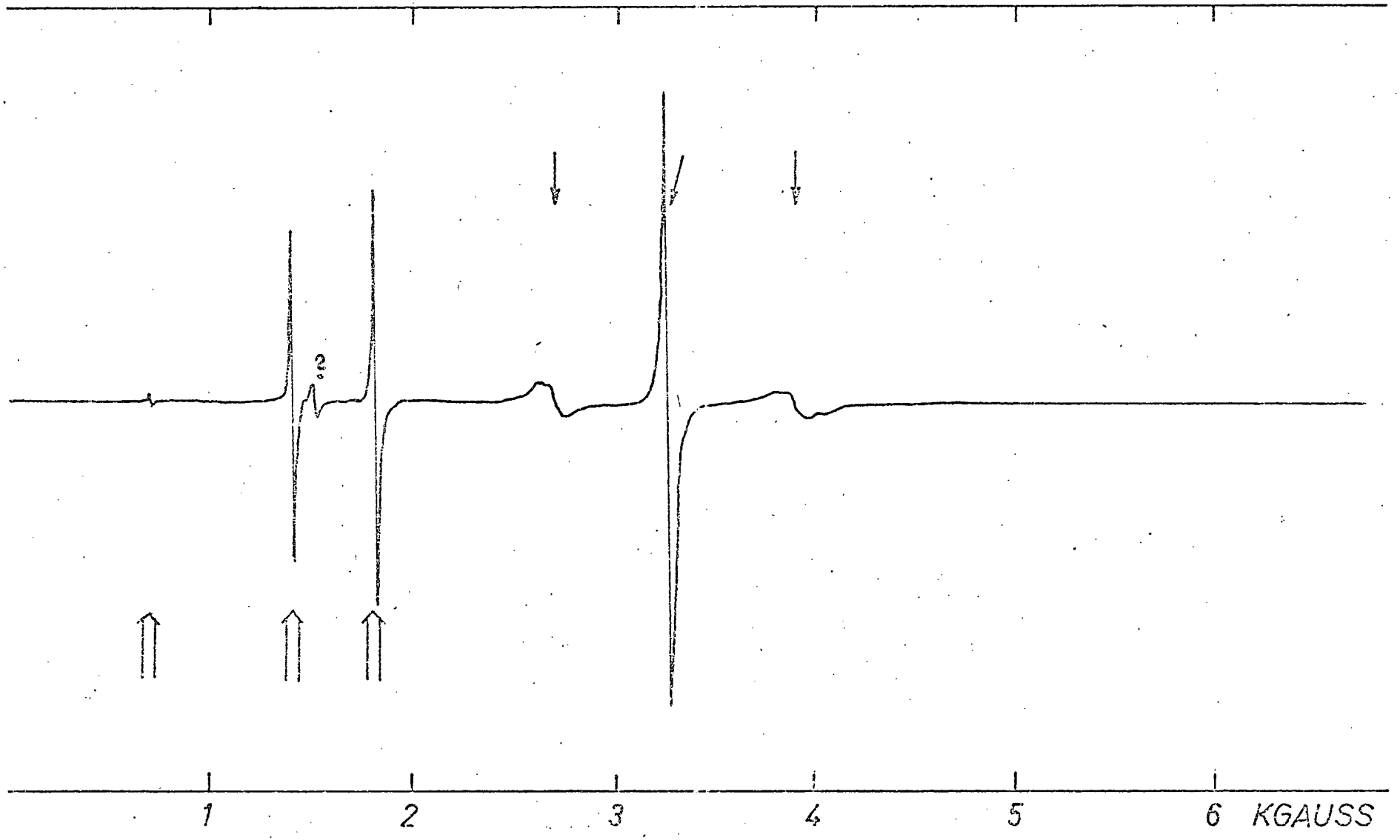

Fig.6 EPR spectrum at X-band of a natural anatase crystal with H parallel to [100] at room temperature

5.2. EPR spectrum I

The five lines marked with single arrows in Fig.5 are called spectrum I. Their angular dependence is shown in Fig. 7 for three crystal planes. This angular dependence, the observability of the spectrum at room temperature, the relative intensities of the five lines and the absence of a hyperfine structure indicate that these lines belong to Fe^{3+} impurities in a crystal field of tetragonal symmetry with respect to the [001] crystal axis.

Using the crystallographic [100], [010] and [001] axes as x, y and z axes respectively, the spectrum could be described by the spin Hamiltonian (7) with parameters given in Table II. These values were obtained by fitting the transition fields with H parallel to [001], [100] and [110] to (7), evaluated to second order. The results were checked by direct diagonalization of the energy matrix with a computer programme. The absolute signs of the spin Hamiltonian parameters were deduced from the relative intensities of the EPR lines at liquid helium temperature. At low temperatures the high field lines were more intense, leading to the identification of the individual fine structure lines as given in Fig.7.

Whereas the spin Hamiltonian (7) with the parameters given in Table II, describes completely the angular dependence of the positions of the lines of spectrum I, it does not

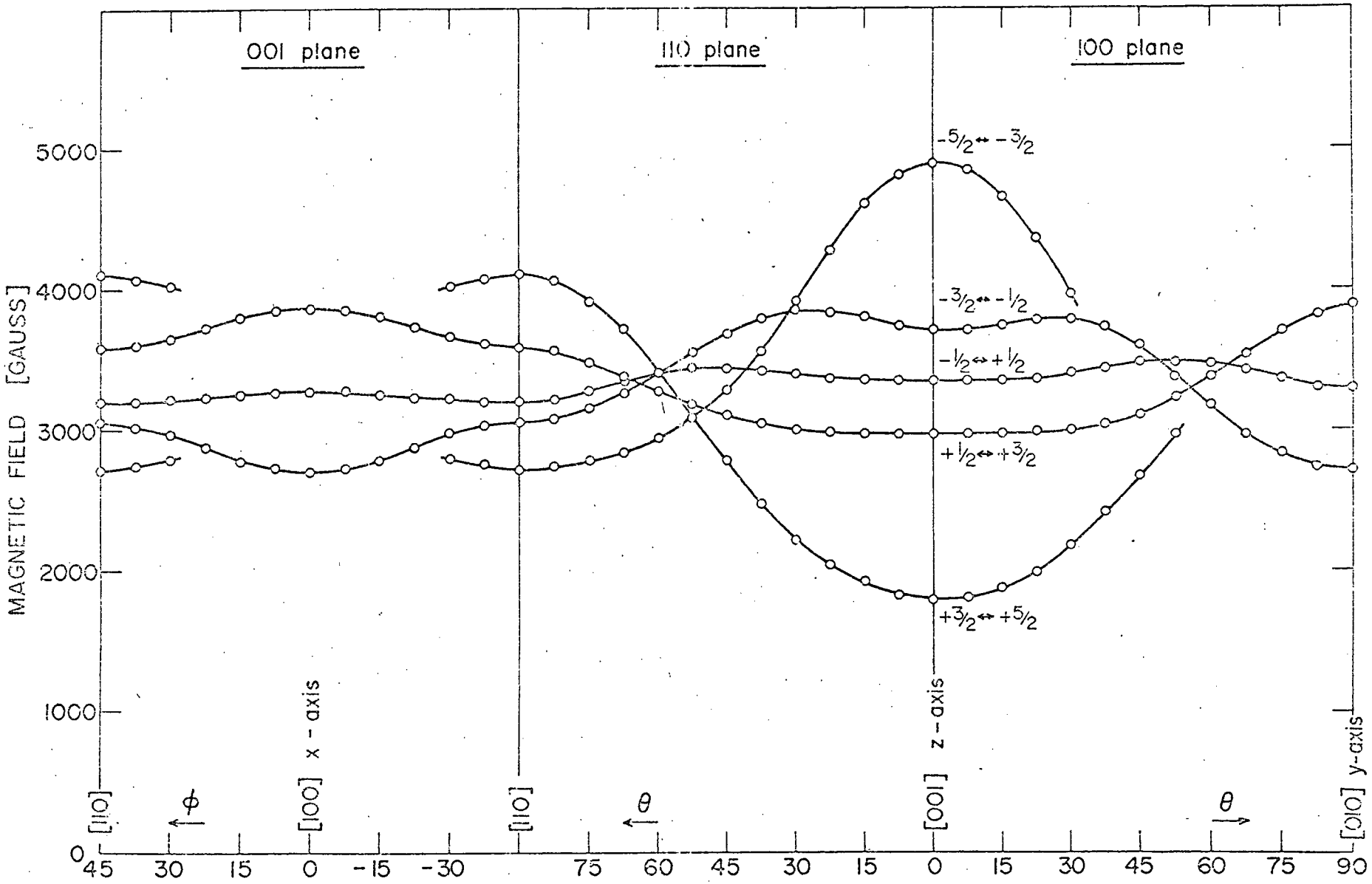

Fig.7 Angular dependence of EPR lines of spectrum I in anatase at X-band with H rotated in three different crystal planes

Table II Spin Hamiltonian Parameters of Spectra I and II in Anatase at 78 °K and 300 °K

All energies are in 10^{-4} cm^{-1}

	Spectrum I (Substitutional Fe^{3+})		Spectrum II (Charge compensated Fe^{3+})	
	78 °K	300 °K	78 °K	300 °K
$g_{\parallel}$	2.004 ± 0.001	2.005 ± 0.001	2.002 ± 0.005	
$g_{\perp}$	2.004 ± 0.002	2.005 ± 0.002		
b_2^0	+ 447 ± 1	+ 308.7 ± 1	- 5110 ± 30	- 4970 ± 30
b_2^2	-	-	- 3540 ± 30	- 3720 ± 30
b_4^0	+ 55.9 ± 1	+ 53.5 ± 1	- 26 ± 10	- 14 ± 10
b_4^2	-	-	+ 60 ± 50	+ 87 ± 50
b_4^4	+ 267 ± 3	+ 257 ± 3	+ 100 ± 10	+ 70 ± 10

explain the angular dependence of the linewidth. In Table III the linewidths for some orientations of H are given.

Table III Linewidths (between Peaks of Derivative Curves) of Spectrum I in Anatase at Room Temperature, in Gauss

Transition	H // [100]	H // [110]	H // [001]
$\|1/2\rangle \leftrightarrow \|-1/2\rangle$	12 ± 2	12 ± 2	12 ± 2
$\|\pm 1/2\rangle \leftrightarrow \|\pm 3/2\rangle$	70 ± 20	12 ± 2	14 ± 2
$\|\pm 3/2\rangle \leftrightarrow \|\pm 5/2\rangle$	unmeasurable	19 ± 3	19 ± 3

The outer fine structure lines are particularly broad when H is parallel to the magnetic x or y axis. This behaviour is indicated in Fig.8. There the peak to peak heights of the outer EPR fine structure lines, normalized to 1 for H // [110], are plotted as a function of the orientation of H in the (001)-plane. The peak heights drop very fast when H is rotated away from the [110] direction. Assuming a constant line shape, these peak heights are a sensitive measure of the linewidths.

This angular dependence of the linewidths cannot be explained with a mosaic structure of the crystal since this would cause a broadening of the lines for intermediate orientations and not for directions along the magnetic axes where the lines have extremum positions.

Formally, this line broadening along the [100] and [010] directions can be described by introducing an orthorhombic term

$$\sigma b_2^2 (S_x^2 - S_y^2) \qquad (16)$$

in the spin Hamiltonian (7), with σ varying randomly between $-1 \leq \sigma \leq +1$ from one paramagnetic centre to the next. This term will inhomogeneously spread out the $|\pm 1/2\rangle \leftrightarrow |\pm 3/2\rangle$ transitions along the x and y axes by $18b_2^2/g\beta$ (calculated to first order) and the $|\pm 3/2\rangle \leftrightarrow |\pm 5/2\rangle$ transitions by $36b_2^2/g\beta$.

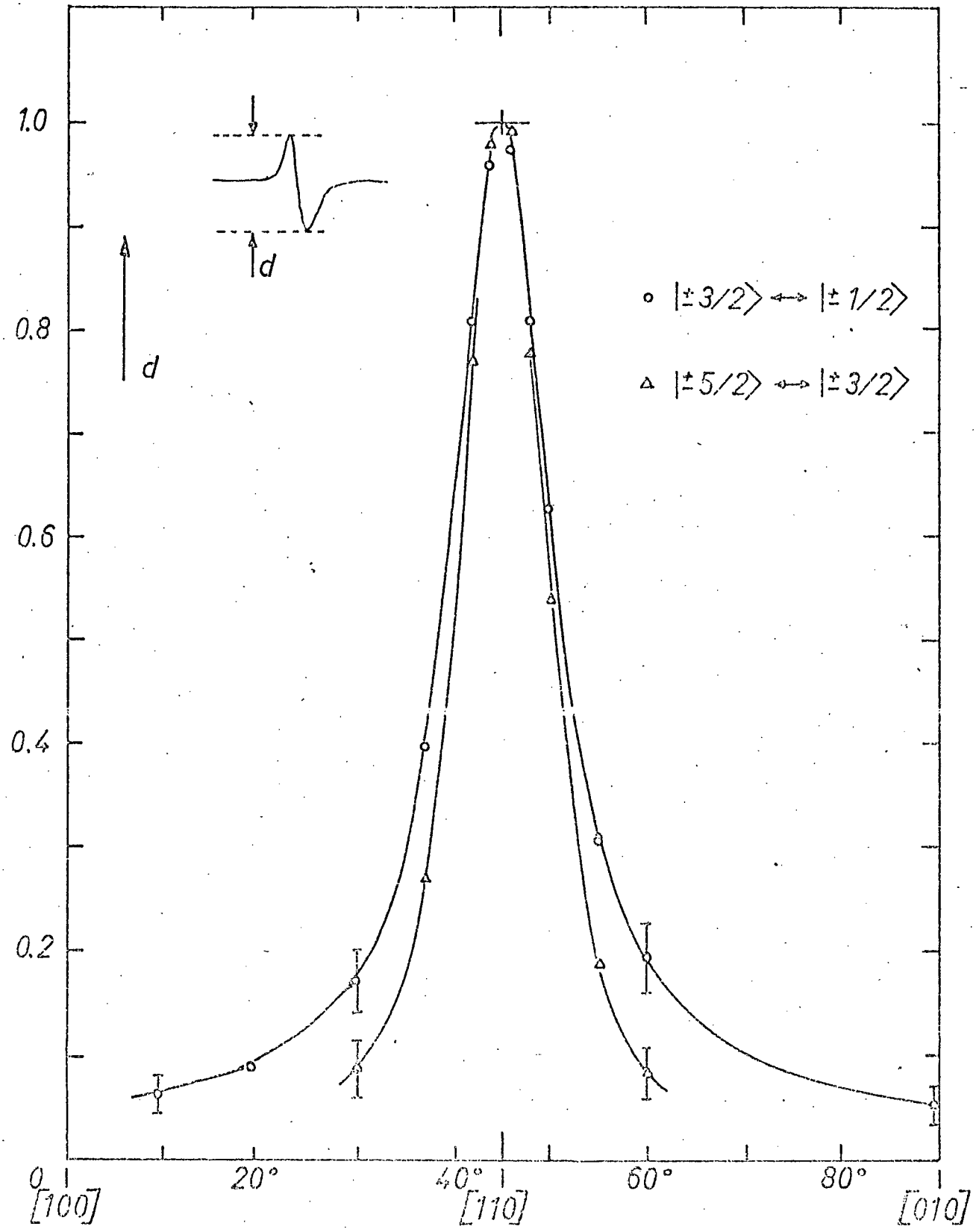

Fig.8 Peak heights of the outer fine structure lines of spectrum I in anatase with H rotated in the (001)-plane, normalized to 1 at H // [110]

but it will not affect the transition fields in the [001] and [110] directions. The linewidth of 70 Gauss of the $|\pm 1/2\rangle \leftrightarrow |\pm 3/2\rangle$ transitions along the x and y axes leads then at room temperature to

$$b_2^2/g\beta = 30 \pm 6 \text{ Gauss.}$$

5.3. Temperature dependence of spectrum I

The positions of the individual lines of spectrum I, with exception of the centre line, depend very strongly on temperature. Fig.9 and Fig.5 show this spectrum for H // [001] for four different temperatures and in Fig.10 the line positions for the same direction of the magnetic field are plotted as a function of the temperature between 1 ^{o}K and 1070 ^{o}K.

The spin Hamiltonian constants at 78 ^{o}K are given in Table II. At this temperature the spectrum shows some saturation. Fig.11 shows the temperature dependence of b_2^{o} and b_4^{o}. Whereas b_4^{o} decreases only slowly with increasing temperature, b_2^{o} decreases from + 457 x 10^{-4} cm^{-1} at 1 ^{o}K almost linearly with temperature over most of the analysed temperature range, passes through zero at 800 $\pm$ 10 ^{o}K and reaches - 225 x 10^{-4} cm^{-1} at 1230 ^{o}K.

The fine structure of spectrum I is also clearly visible with H // [110] up to high temperatures as can be seen in Fig.12, whereas the broad $|\pm 1/2\rangle \leftrightarrow |\pm 3/2\rangle$ transi-

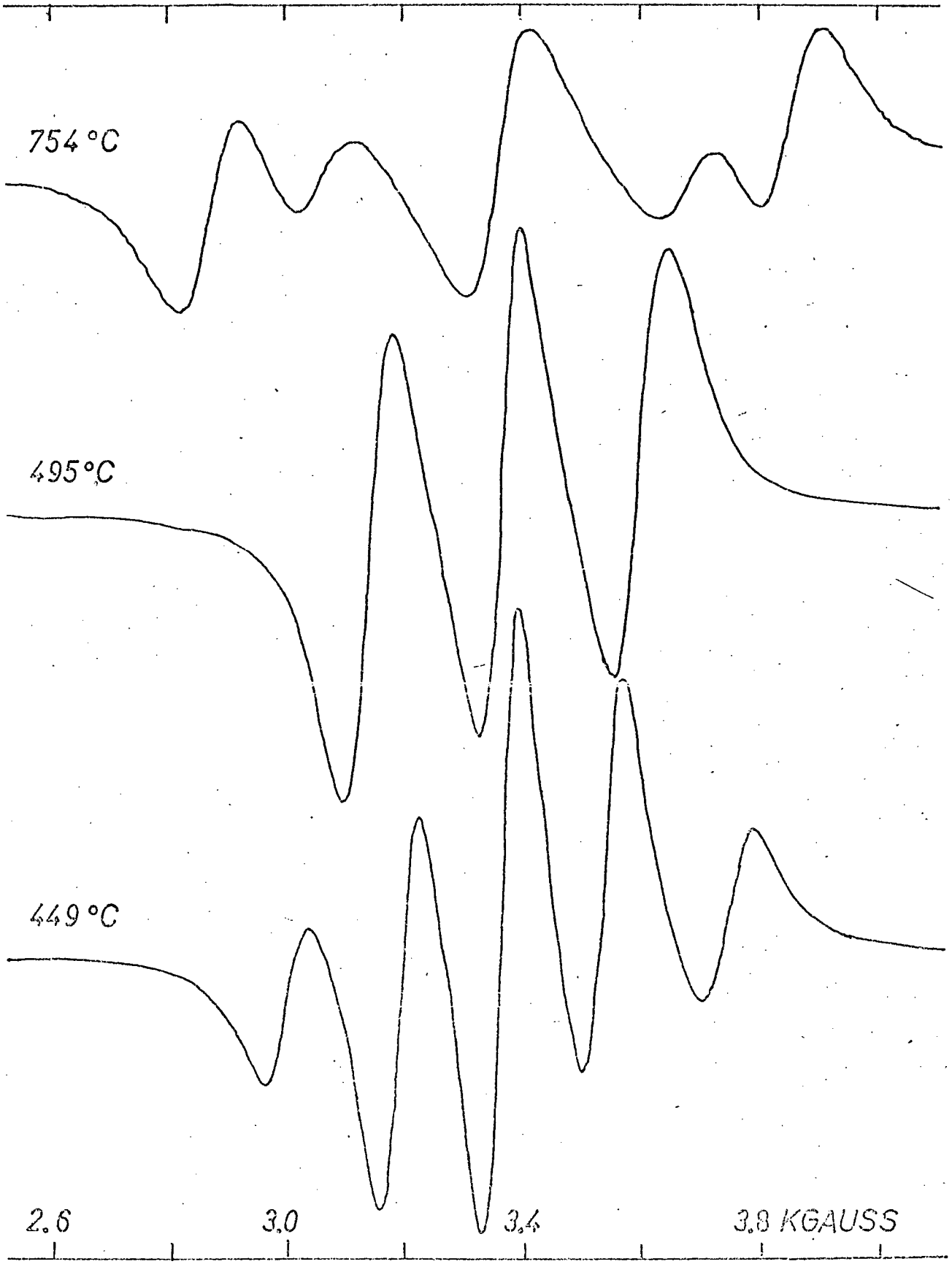

Fig.9 EPR spectra at X-band of a natural anatase crystal with H parallel to [001] at 449 °C, 495 °C and 754 °C

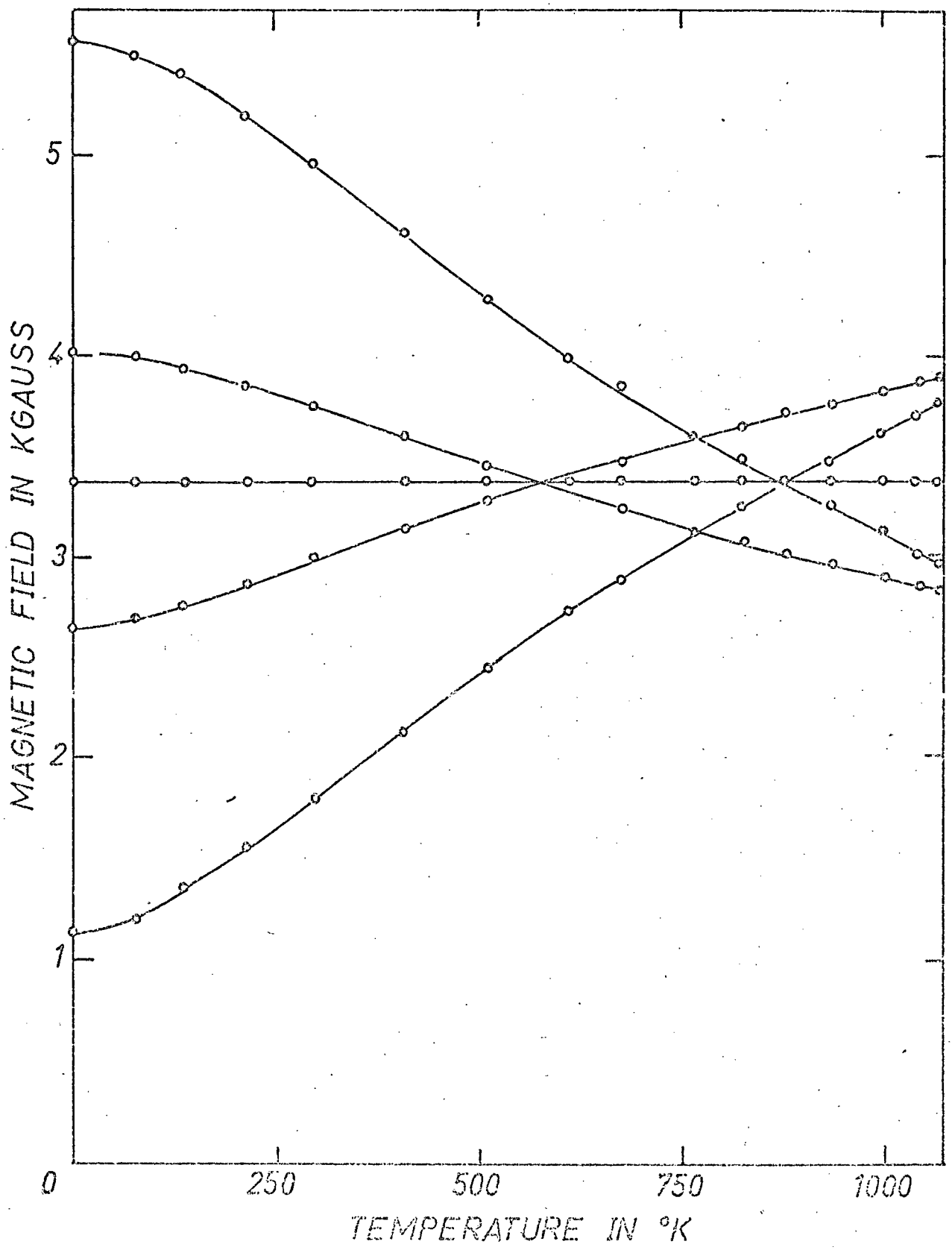

Fig.10 Temperature dependence of EPR lines of spectrum I at X-band of anatase with H parallel to [001] as a function of temperature

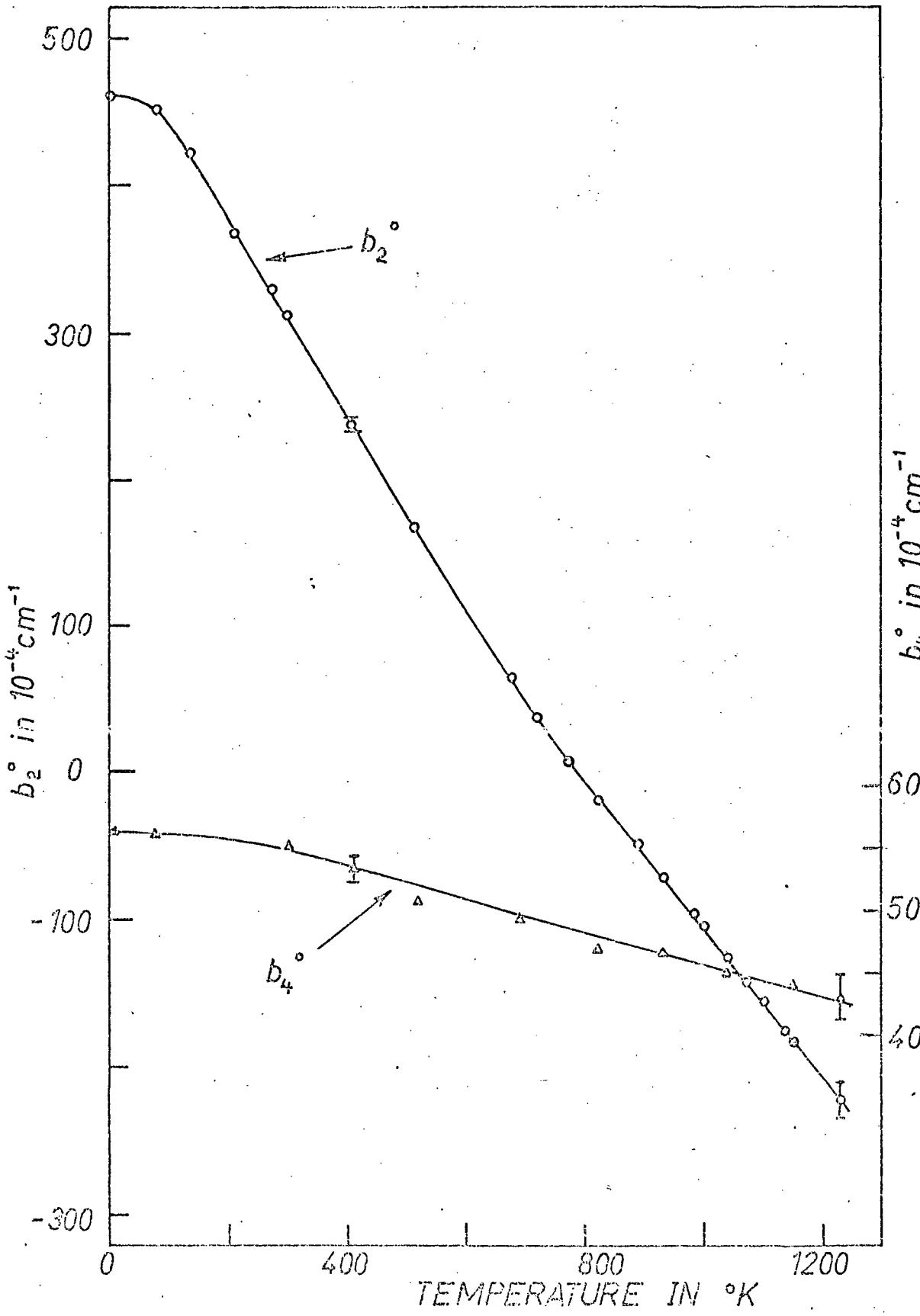

Fig.11 Temperature dependence of b_2° and b_4° of spectrum I in anatase

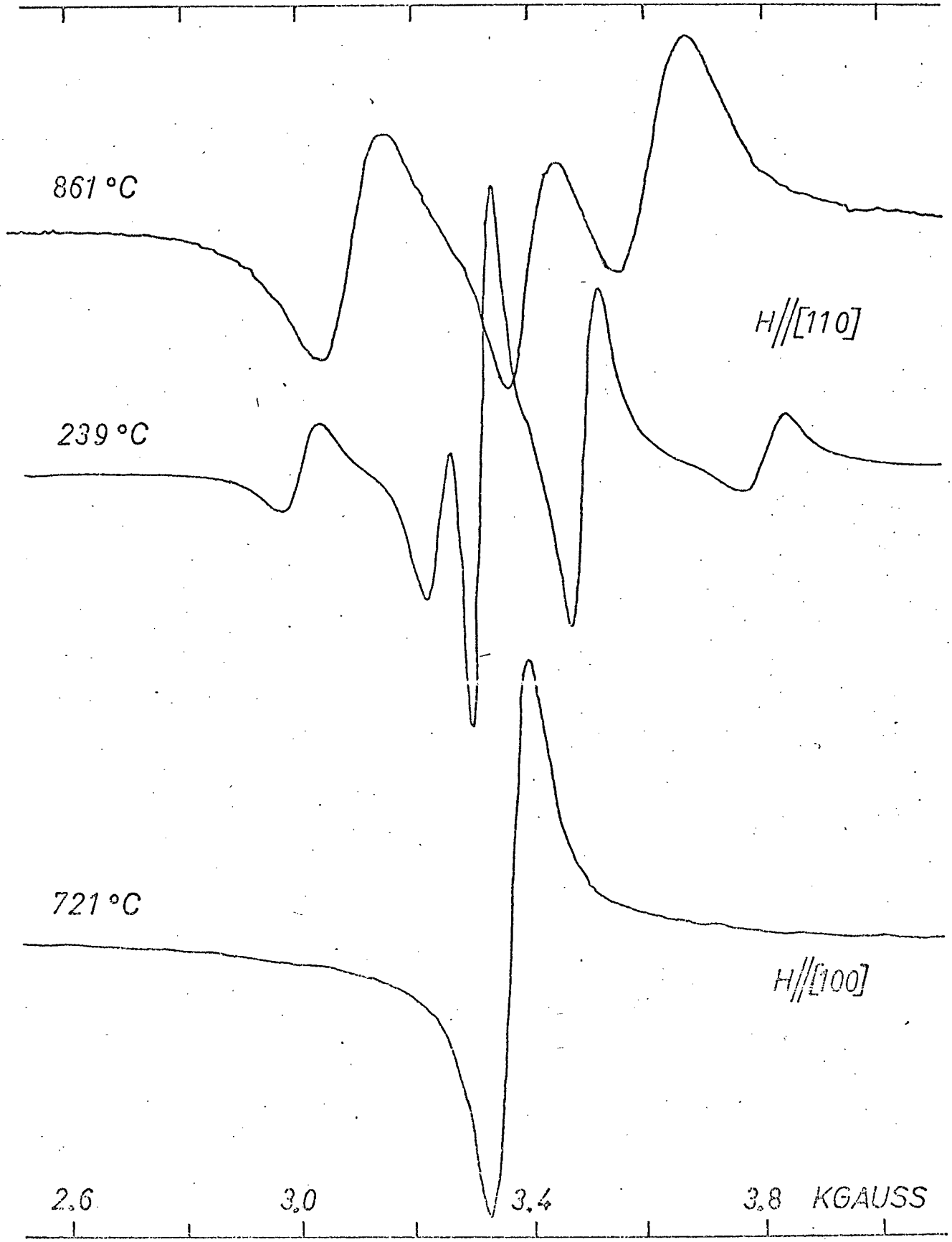

Fig.12 EPR spectra of a natural crystal at X-band with H parallel to [110] at 239 °C and 861 °C and with H parallel to [100] at 721 °C

tions with H//[100] broaden with increasing temperature still more, so that at higher temperatures only the centre transition is visible. One recording for this direction is included in Fig.12. This broadening indicates that b_2^2 in the random orthorhombic term (16) increases with temperature. In addition, the spectrum has no cubic symmetry at 800 ^{o}K, where $b_2^o = 0$, since the spectra for H//z and H//x (or y) are different.

At the highest analysed temperature, 1230 ^{o}K, the anatase crystal already began to transform to rutile. Within 30 min. the intensity of spectrum I decreased to about one half of its initial value. The transformation to rutile started on the surface of the crystal and the transformed part was milky-yellow, opaque and under the microscope appeared polycrystalline.

5.4. EPR spectra II

In addition to the EPR lines of spectrum I, one observes in the anatase crystals other rather intense EPR lines. They are marked in Fig.5 and 6 with double arrows. These lines are characterized by a large anisotropy and strong angular dependent intensities. Fig.13 shows in the upper part the angular dependence of these lines in the (100)-crystal plane at room temperature and 9.19 GHz. The intense lines between 1383 Gauss and 1783 Gauss have a line-width of 11 - 14 Gauss.

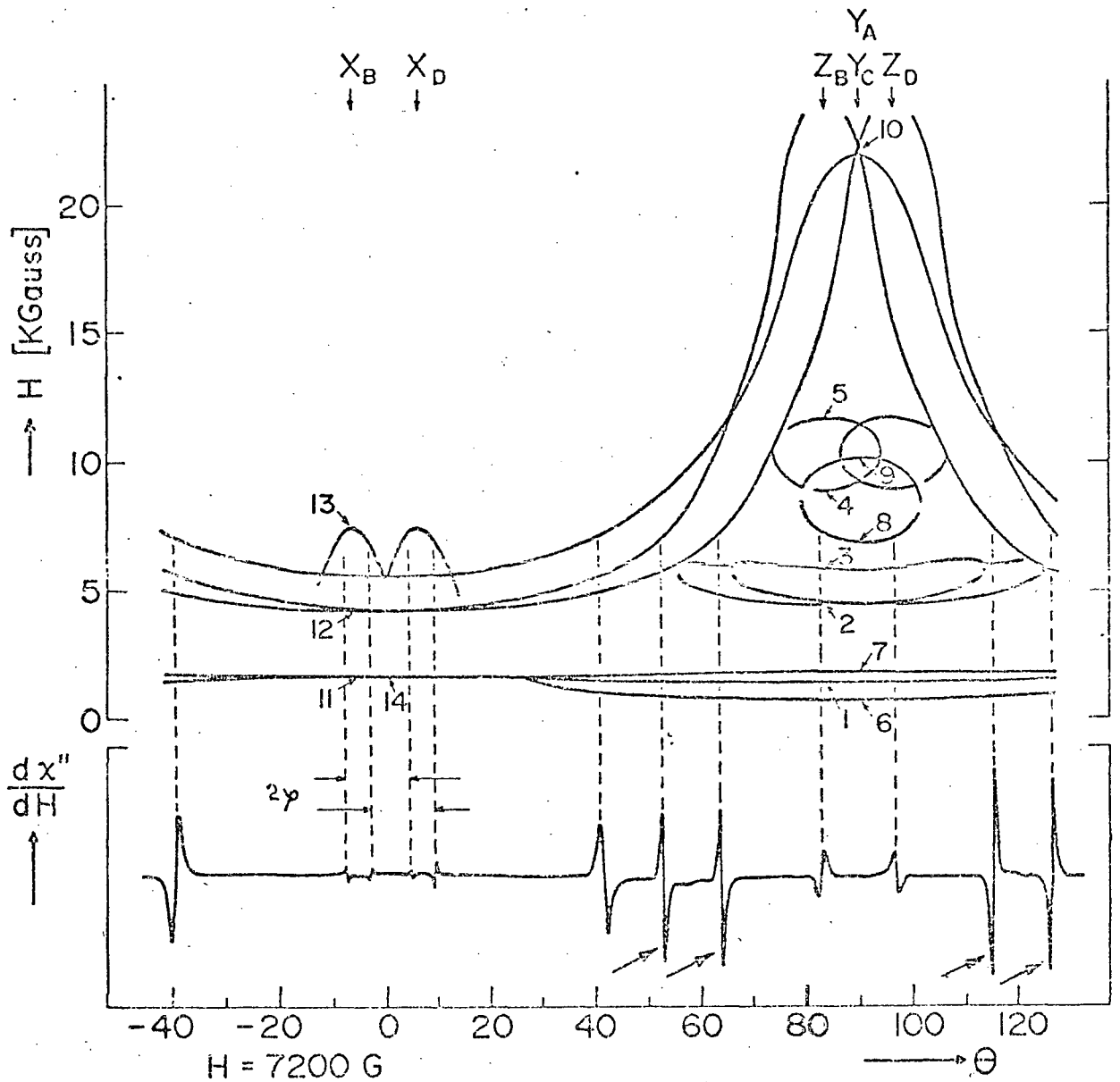

Fig. 13 Spectra II in the (100)-crystal plane of anatase at room temperature and 9.19 GHz. 23 KGauss was the highest obtainable field. The lower part of the figure shows a spectrum obtained by rotating the crystal in the (100)-plane at a constant field H = 7200 Gauss

These lines can be divided into four separate spectra which only differ from one another in 90° rotations of their magnetic axes about the [001]- crystal axis. These four spectra are designated spectra II_{A-D}. The magnetic axes of these spectra, expressed in polar coordinates, are given in Table IV. The absolute accuracy of these directions is $\pm 1^{\circ}$.

Table IV Directions of the Magnetic Axes for Spectrum II_A, Expressed in Polar Coordinates (θ, ϕ). The Axes of the Other Three Spectra II are Obtained by Successive Rotations of 90° about the [001] Crystal Axis.

Magnetic axis	Direction in crystal (θ, ϕ)
x	(φ, 180°)
y	(90°, 90°) $\hat{=}$ [010]
z	(90° - φ, 0°)

300 °K: $\varphi = 6.32 \pm 0.01^{\circ}$

78 °K: $\varphi = 6.15 \pm 0.01^{\circ}$

At the top of Fig.13 are indicated these magnetic axes which lie in the (100)-plane. y_A means the y-axis of spectrum II_A, etc.

The lower part of Fig.13 shows a spectrum obtained by rotating the crystal at a constant field H = 7200 Gauss in the (100)-plane. From this spectrum one deduces directly

an accurate value for φ, the angle which is included in the specification of the magnetic axes as given in Table IV.

Spectra II, as spectrum I, are caused by iron impurities in the anatase crystal. This is confirmed by the EPR analysis of the synthetic powders. Fig.14 shows the EPR spectrum of anatase powder doped with 1 mol-% of Fe. The three EPR powder lines marked with arrows correspond to the strong lines in the single crystal at 1617, 1783 and 1383 Gauss with H along the x, y and z axes, respectively. These EPR lines are not found in pure anatase powder, nor anatase doped with Cr or Mn.

The intensity, the linewidths and the absence of a hyperfine structure, together with the powder analysis, indicate that spectra II are also produced by ferric iron in a high spin state ($S = 5/2$). From the strong anisotropy of the lines and the absence of a line near $g = 2$, one can however infer that the zero splitting is large compared to the Zeeman energy at X-band. The quadrupolar terms b_2^m in the spin Hamiltonian (3) therefore have to be dominant and their principal axes will determine the orientations of the magnetic axes. Hence, an isotropic $g = 2.0023$ was assumed and initially all b_4^m were set equal to zero.

A first guess for the remaining b_2^0 and b_2^2 was obtained by using graphs given by Troup et al.[51] and Aasa[52], as discussed in Appendix B. Troup et al.[51] calculate the

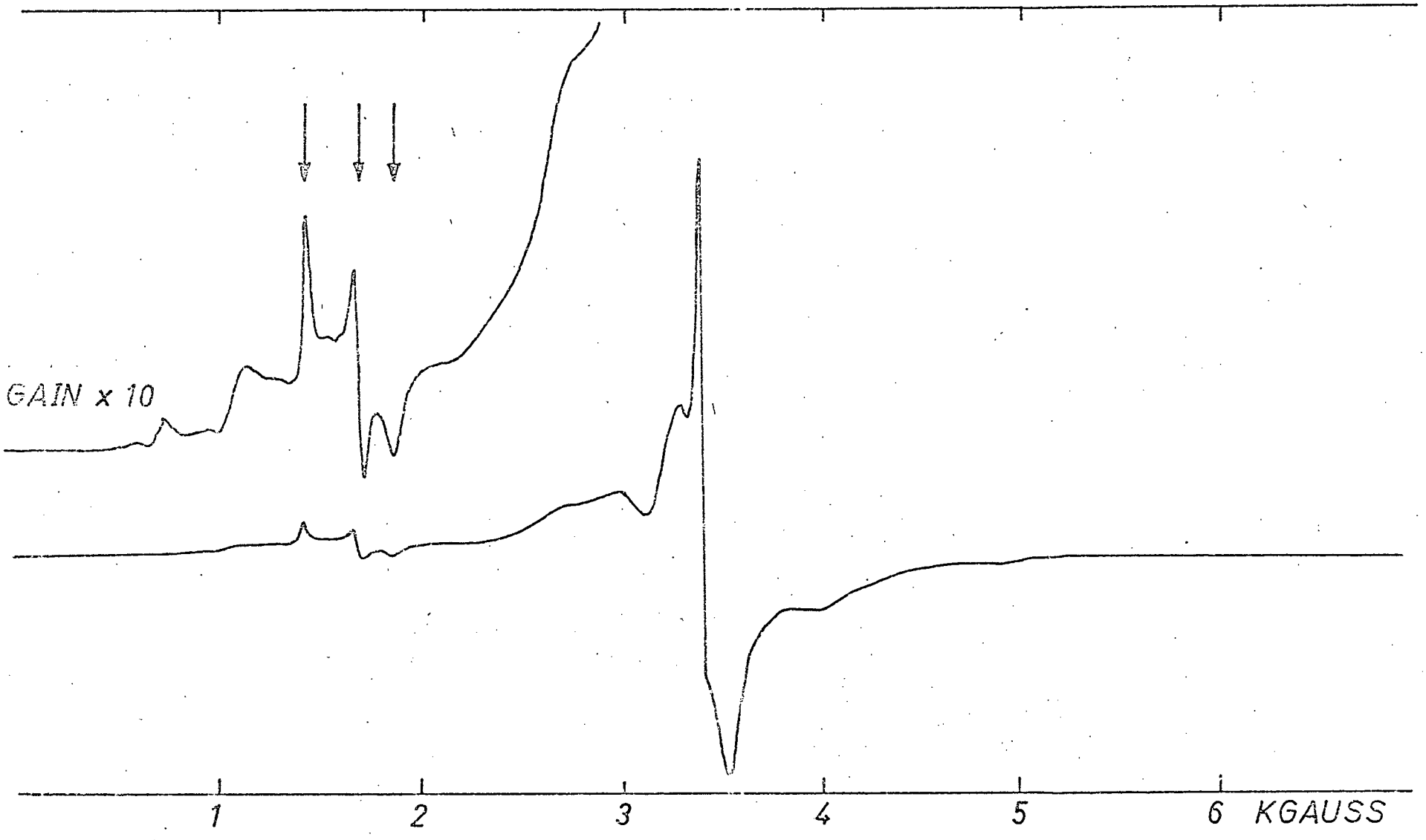

Fig. 14 EPR spectrum at X-band and room temperature of synthetic anatase powder doped with 1 mol-% of Fe

effective g value for the EPR transitions within the three ground state doublets of Fe^{3+} in a strong crystal field ($D/h\nu \gg 1$) as a function of $E/D = b_2^2/3b_2^0$. With the observed transitions in anatase one obtains $E/D = 0.25 \pm 0.02$. The axes in Table IV are already chosen to give a fit with $0 \leq b_2^2/b_2^0 \leq 1$. The next step was to use this value of E/D and the graphs of Aasa[52], who calculated for Fe^{3+} the transition fields H versus D, using E/D as a parameter. The result was $D = 14.2 \pm 1$ GHz. An adjustment of these parameters was then made with a computer programme given by J. Hebden et al.[53], using a trial and error method. This programme calculates, for given b_2^0 and b_2^2, the EPR transition fields and plots the energy levels. Fig.15 shows the results for the cases with H parallel to the three magnetic axes. The observed transitions are indicated and marked identically as in Fig.13.

A final least mean square computer calculation of b_2^0, b_2^2 and including b_4^0, b_4^2 and b_4^4 in the spin Hamiltonian, was made to fit all 13 EPR lines in Fig.13. This method is discussed in Appendix C. The results are included in Table II. The absolute signs of the b_n^m were again established with an EPR measurement at liquid helium temperature.

It should be pointed out that the b_4^m of Table II are only an order of magnitude estimate, since there exists no reason to suppose that the principal axes of the tensor b_4^m coincide with the principal axes of b_2^m, the latter being taken as

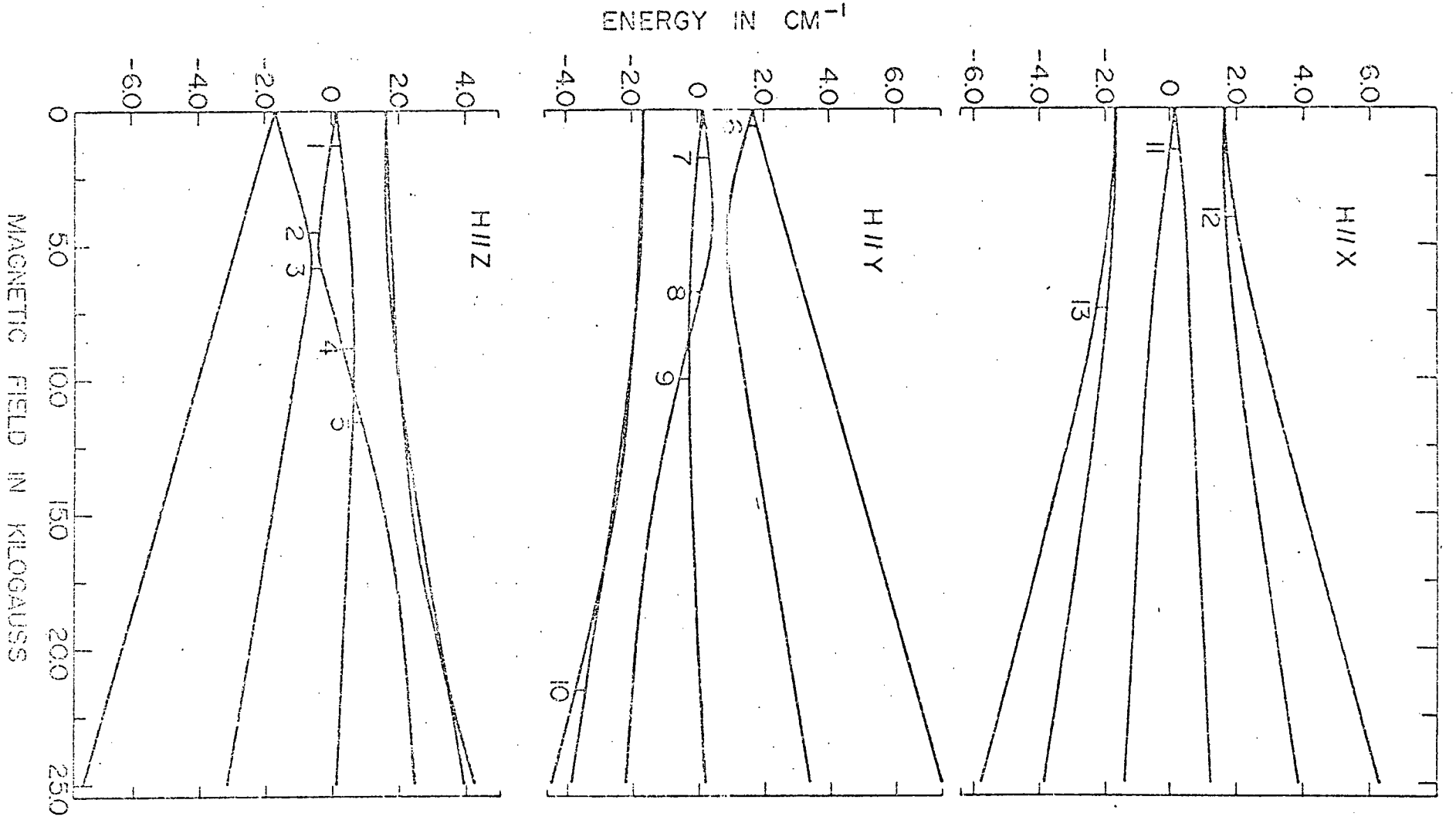

Fig. 15 Energy levels of a paramagnetic centre II in anatase with H parallel to each of the three magnetic axes. The observed transitions are indicated and numbered as in Fig.13

defining the magnetic axes. But by including b_4^0, b_4^2 and b_4^4 the calculated transition fields agree with the measured ones to within the experimental error, which is ca. 0.1%, and an additional inclusion of b_4^1 and b_4^3 in the spin Hamiltonian did not seem warranted.

In order to obtain an estimate of the relative spin concentration of centres of type I and II, the spectra at room temperature with H parallel to the [001]-axis were used (Fig.5). Along this direction the four spectra II coincide and the line intensities A_I of the centre line $|+ 1/2\rangle \leftrightarrow |- 1/2\rangle$ of spectrum I and A_{II} of the $|+ 3/2\rangle \leftrightarrow |- 3/2\rangle$ line of spectra II (line No.14 of Fig.13) were compared. The high field nomenclature $|\pm 3/2\rangle$ is used here only to identify these two states as belonging to the intermediate Kramers doublet of centre II. The relative spin concentration is given by

$$\frac{N_{II}}{N_I} \approx \frac{N_{II,i}}{N_{I,i}} = \frac{A_{II}}{A_I} \cdot \frac{|\langle i | S_{100}^{I} | f \rangle|^2}{|\langle i | S_{100}^{II} | f \rangle|^2} \qquad (17)$$

where $N_{I,II}$ is the total number of spins I, II in the sample, $N_{I,II,i}$ is the number of spins I, II in the state $|i\rangle$, and $|\langle i | S_{100}^{I,II} | f \rangle|^2$ is the induced transition probability between states $|i\rangle$ and $|f\rangle$ for the microwave magnetic field parallel to [100].

Using

$$|\langle 1/2 \mid S^{I}_{100} \mid -1/2\rangle|^2 = 9/4$$

$$|\langle 3/2 \mid S^{II}_{100} \mid -3/2\rangle|^2 \approx 4.4 \quad \text{(ref.54)}$$

a value $N_{II}/N_I = 0.3 \pm 0.1$ is obtained. This means that in the analysed crystals for each paramagnetic centre of type II there exist some 3-5 centres of Type I.

5.5. Temperature dependence of spectra II

The spin Hamiltonian parameters which describe spectra II were in addition determined for 78 ^{o}K using the same procedure as discussed in the previous section. The results are also included in Table II. At this lower temperature the orthorhombic term b_2^2 is smaller, whereas b_2^o is larger than at room temperature.

Spectra II show only a small saturation effect even at 1 ^{o}K. On the other hand, if the temperature is raised above room temperature the lines broaden and for temperatures higher than + 300 ^{o}C the spectra become unobservable.

Special attention has been given to an accurate measurement of the angle φ, determining the orientation of the magnetic axes of spectra II. The weak lines between $\theta = \pm 20^{o}$ in the spectrum shown in the lower part of Fig.13 were used to measure the angle φ. These lines belong pairwise to transitions

in the lowest Kramers doublets of spectra II_B and II_D (near line No.13 of Fig.15) and are particularly appropriate for an accurate measurement of φ. First, they are near $\theta = 0(H//[001])$, an orientation which can be achieved accurately because there the four spectra of type II coincide, thus giving a check for the correct orientation of the crystal in the magnetic field H. Second, the separation between these lines does not change measurably for small rotations of the crystal out of the (100)-plane. The results at 300 ^{o}K and 78 ^{o}K are given in Table IV. At the lower temperature φ is slightly smaller.

The weak lines used to determine φ at 300 ^{o}K and 78 ^{o}K could not be followed to higher temperatures. Therefore, the strong transitions in the highest Kramers doublets of II_B and II_D, marked with arrows in the spectrum of Fig.13, were used above room temperature. These transitions occur, however, at intermediate angles θ where no reference orientation exists to align exactly the crystal and, in addition, the separation between these lines changes markedly if the magnetic field is rotated slightly out of the (100)-plane. Consequently, the separation between these lines, now designated $2\varphi'$, is shown in Fig.16. It indicates only qualitatively the temperature dependence of the directions of the magnetic axes. These angles differ by about 1^{o} from 2φ as given in Table IV.

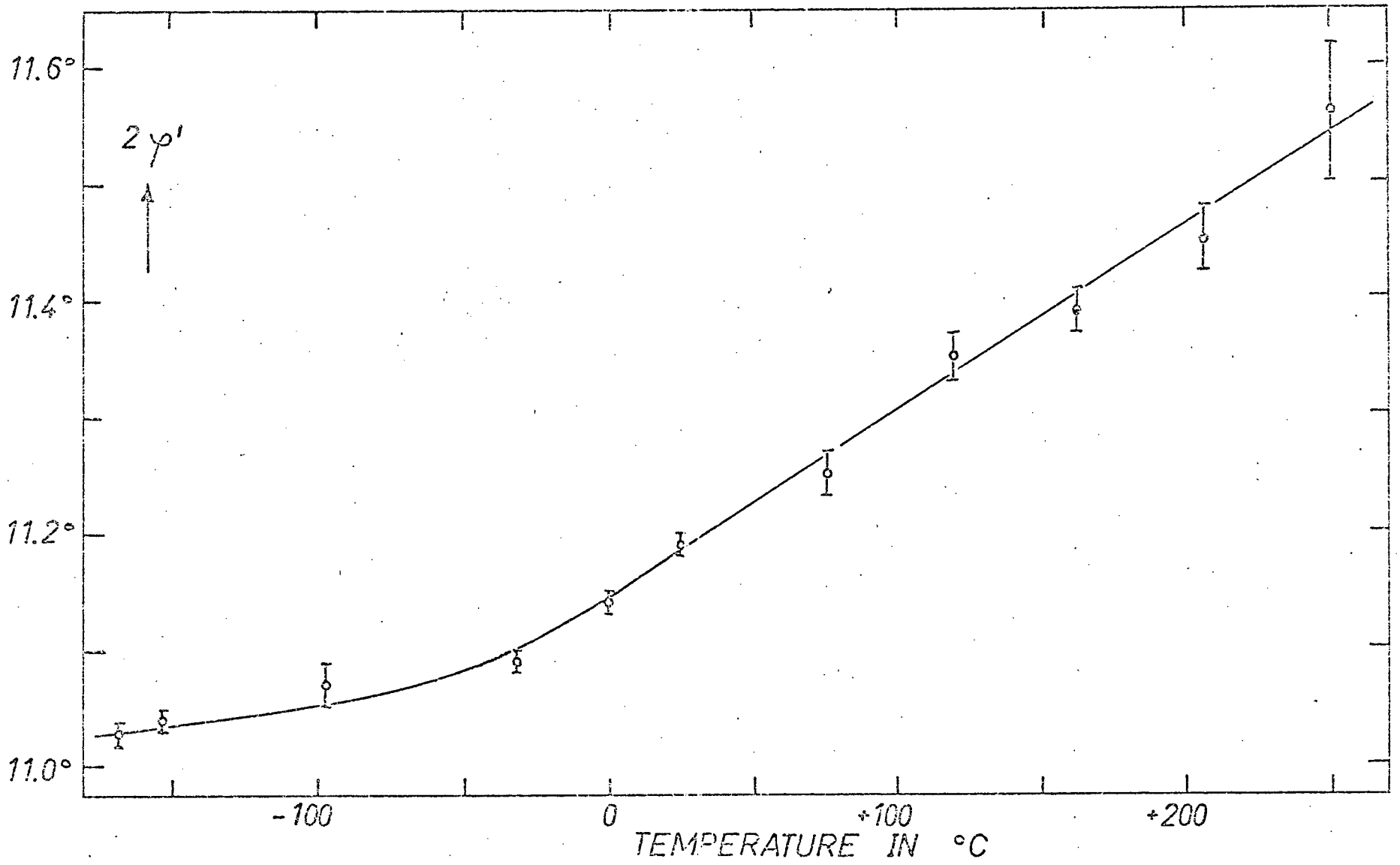

Fig.16 Temperature dependence of the angle $2\varphi'$, as defined in the text. Approximately φ' gives the magnetic axes of the four spectra II, defined in Table IV

6. DISCUSSION OF RESULTS

6.1. EPR spectrum I: substitutional Fe^{3+}

As discussed in section 2.1., all Ti^{4+} sites in anatase have $\bar{4}2$ point symmetry. If Fe^{3+} substitutes for Ti^{4+} then a single paramagnetic spectrum with tetragonal symmetry along the [001]-axis is expected. Spectrum I is interpreted as resulting from such a centre.

From the symmetry of the spectrum it is also possible that the Fe^{3+} ions are at interstitial sites such as I in Fig.1. However, this would generate a strong local charge inequality. In addition, in rutile one observes paramagnetic impurities in the larger interstitial sites only if the impurities are too large to enter the substitutional site[6]. In rutile these sites are distinguishable because they have other symmetry axes than the substitutional sites. In anatase, however, the four nearest neighbour distances are the same for the interstitial as for the substitutional sites and, in octahedral coordination, the ionic radius of Fe^{3+}, 0.73 Å, is also nearly the same as that of Ti^{4+} (0.69 Å) [14]. Thus one can conclude that the Fe^{3+} ions enter anatase substitutionally.

There exist two main differences between the EPR spectra of substitutional Fe^{3+} in anatase and in rutile[55,56]: the zero field splitting is smaller by a factor of 20 in anatase and, contrary to the case of rutile, is strongly sensi-

tive to temperature. These differences are surprising because the structure and physical properties of the two crystals are very similar.

An attempt was made to calculate the spin Hamiltonian parameter b_2^0 following the ideas of Sharma et al.[43], as discussed in section 3.2. For this purpose the lattice sums B_2^0 and $(B_4^0)'$, defined in (12) and (13), were calculated with a point charge model of anatase, using the crystallographic data of (1). The sums were carried out with a computer programme over all ions within a sphere of 20 Å, 30 Å and 40 Å around a Ti^{4+} ion site. The results for the two larger spheres differ less than 1%, indicating a good convergence of the lattice sums (a sphere with a radius of 40 Å includes some 25,000 ions). The results are

$$B_2^0 = + 154 \times 10^{-4} \; e^2/2a_o^3$$

$$(B_4^0)' = + 4.2 \times 10^{-4} \; e^2/2a_o^5$$

Introducing these values in (11) results in $b_2^0 = + 8.2 \times 10^{-4}$ cm^{-1} which compares with the experimental value $b_2^0 = + 308.7 \times 10^{-4}$ cm^{-1}. Since the numerical factors in (11) were calculated for Mn^{2+} in ZnF_2, they will not apply exactly in our case, but the same order of magnitude would be expected for Fe^{3+}. One possible explanation for this discrepancy is the high polarisibility of anatase. This would result in a deformation of the neighbouring oxygen ions and a change of

their positions when replacing Ti^{4+} by the smaller charge of Fe^{3+}.

This discrepancy between calculated and measured b_2^o exists also in rutile where a point charge calculation gives $B_2^o = -45 \times 10^{-4}\ e^2/2a_o^3$, $(B_4^o)' = -251 \times 10^{-4}\ e^2/2a_o^5$, with the z axis parallel to [110]. No explanation for the large differences of the observed zero field splitting of Fe^{3+} in anatase and rutile can therefore be deduced from these calculations.

Nevertheless, the point charge model seems adequate to explain qualitatively the temperature dependence of the spin Hamiltonian parameters in anatase. In the calculation of the lattice sums B_2^o and $(B_4^o)'$ it was found that they are very sensitive to small changes in the oxygen parameter u (see Fig.1). The results are given in Fig.17. An increase of u from 0.413 Å, its value at room temperature, to 0.452 Å decreases B_2^o to zero and $(B_4^o)'$ to $-7.3 \times 10^{-4}\ e^2/2a_o^5$. At first glance, this result is surprising in as much as an increase of u deforms still more the oxygen octahedron surrounding Ti^{4+}. But the displacements of the oxygen ions A-D (see Fig.1) have an opposite effect on B_2^o than the displacements of the ions E and F.

It was concluded that the temperature dependence of the spin Hamiltonian parameter b_2^o is produced by an increase of the oxygen parameter u with temperature. Also

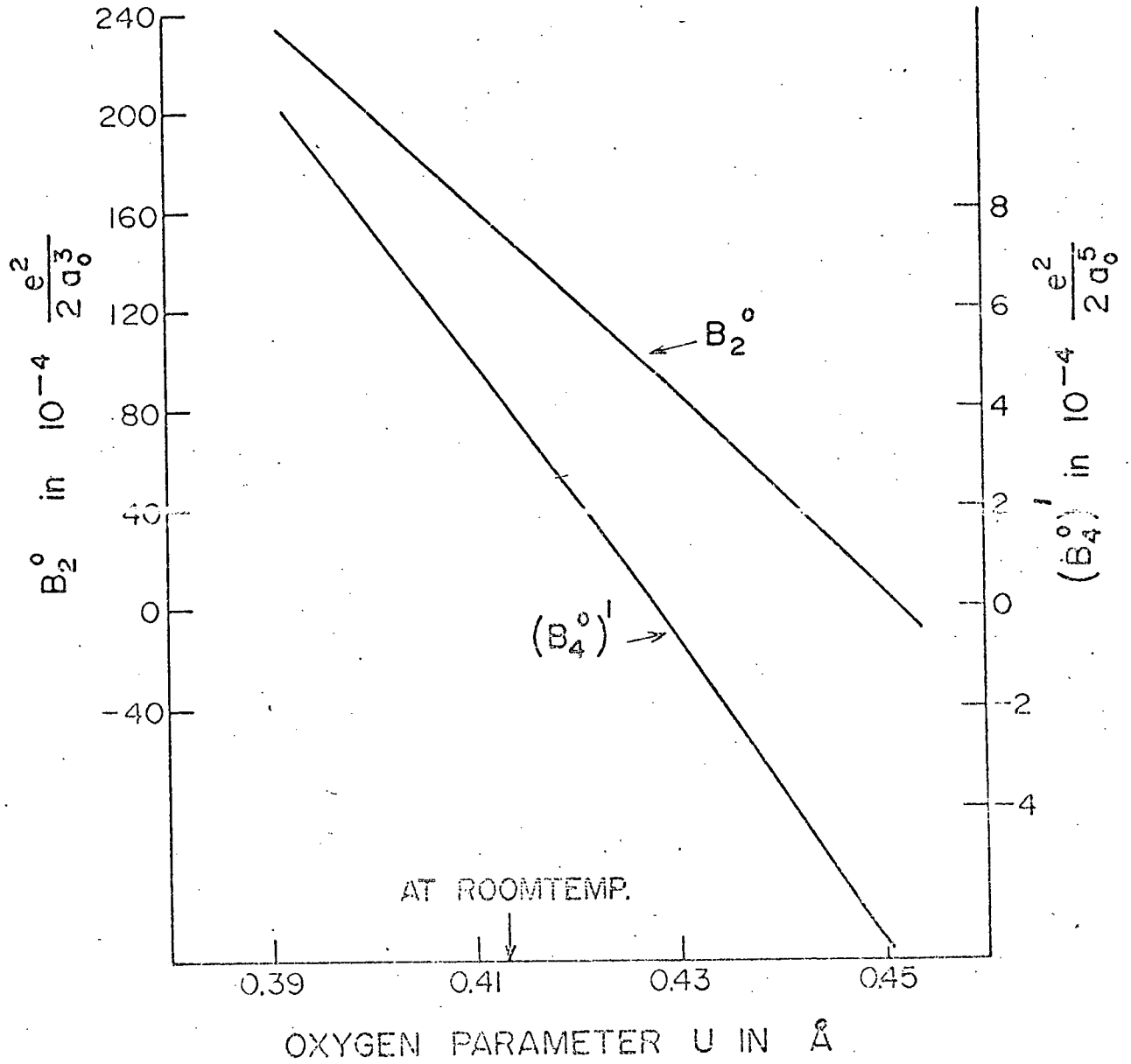

Fig.17 Lattice sums B_2^0 and $(B_4^0)'$, calculated with a point charge model of anatase as a function of the oxygen parameter u

in support of this argument is the temperature dependence of the orientations of the magnetic axes of spectra II as will be discussed below in section 6.2.

This shift of the oxygen ions does not change the symmetry of the crystal. It changes essentially only the bond angles but not the bond lengths between a Ti^{4+} ion and its four nearest oxygen ions. In rutile this is not possible. There, a change of the oxygen parameter affects directly the nearest neighbour $Ti^{4+} - O^{2-}$ distance and hence results in a larger change of the crystal energy. This would explain the absence of the strong temperature dependence of the EPR spectra in rutile.

Unfortunately, no high temperature crystallographic X-ray data of anatase are available in order to check this proposed temperature dependence of the oxygen parameter u. An attempt was made to determine at high temperature the crystal structure of anatase with an X-ray single crystal study using a high temperature Weissenberg camera and - counter, constructed by E. Meagher of the Geology Department of U.B.C. It appeared that the investigation would be too lengthy, mainly because of the involved experimental difficulties, to be included in this thesis.

More insight into the origin of the temperature dependence of b_2^o could be gained if the isothermal pressure dependence of b_2^o were known. This would permit the calcula-

tion of the implicit part of the temperature dependence of b_2^o with (14). Evidently, the proposed temperature dependence of the oxygen parameter u does not correspond to an isotropic thermal expansion, which, according to (15), would result in an increase of b_2^o with temperature. The implicit temperature dependence of b_2^o as given by Walsh et al.[46] in the second term on the right-hand side of (14) should therefore be split into two parts to correspond to the tetragonal symmetry of anatase. One part with the pressure applied parallel to the optical axis and one with the pressure, perpendicular to it.

According to Fig.11, b_4^o decreases 12.5% by increasing the temperature 500 °C. Neglecting the small correction F in (5), this implies that the cubic constant a should also decrease 12.5%. This can be explained by the implicit term given in (15), if an increase in the interionic distances of 0.6% is used. This is consistent with the increase of the lattice parameter c as measured by Rao[25]. One can conclude that the temperature dependence of the spin Hamiltonian parameter a is mainly given by the average increase of the interionic distances and is not affected by minor distortions which, on the other hand, affect strongly the second order term b_2^o.

The lattice sums calculations, using a point charge model of anatase, may also explain the strong broadening of the outer fine structure lines of the EPR spectrum I when the magnetic field is parallel to {100}. For this purpose the

lattice sums B_2^0, $(B_4^0)'$ and

$$B_2^2 = \sqrt{\frac{3}{2}} \sum_j q_j \sin^2 \theta_j \cos 2\phi_j / R_j^3 \qquad (18)$$

were calculated at points along the z axis. The result was again surprising: a displacement of 0.02 Å from the centre of the oxygen octahedron along the z axis changes B_2^0 less than 1% but the generated orthorhombic component B_2^2 already reaches $12 \times 10^{-4}\ e^2/2a_o^3$. Random, stress induced displacements of the Fe^{3+} ions along the z axis by 0.02 Å or less could thus explain the observed angular dependence of the fine structure linewidths. These displacements are so small that the nearest oxygen ion along the z axis would still be farther away from the Fe^{3+} ion than the four nearest neighbours at A-D of Fig.1. Whereas this is one possibility, other random deformations of the crystal structure or displacements of the Fe^{3+} ions could have the same effect on the linewidths.

It is perhaps appropriate for completeness to state that the temperature dependence of spectrum I, measured up to 960 °C, does not show any discontinuity at 642 °C, where Schroeder[26] (cf section 2.3) proposed a reversible phase change to a high temperature form of anatase.

6.2. EPR spectra II: charge compensated Fe^{3+}

Replacement of a Ti^{4+} ion by a Fe^{3+} ion causes a negative charge excess of one elementary charge. This excess

has to be compensated to keep the crystal electrically neutral. The charge compensation can be accomplished in different ways, e.g. other impurities, interstitial ions or oxygen vacancies (V_o - centres). These may be randomly distributed over the crystal or in a fixed geometrical relation to the Fe^{3+} ions.

The most reasonable explanation for the spectra II is that they originate from $Fe^{3+} - V_o$ centre pairs, produced by Fe^{3+} ions at Ti^{4+} sites with charge compensating oxygen vacancies at one of the four nearest neighbour sites. This explains the four spectra II (vacancies at A-D of Fig.1), their symmetries and the directions of their magnetic axes.

Similar EPR spectra of charge compensated Fe^{3+} have been observed in other crystals, e.g. $SrTiO_3$ [57], which has the same basic structural blocks of TiO_6 octahedra. In fact, there exists a remarkable similarity between the EPR spectra of Fe^{3+} in anatase and in the tetragonal low temperature phase of $SrTiO_3$. b_2^0 of normal substitutional Fe^{3+} in $SrTiO_3$ is also strongly temperature dependent and, as will be discussed below for anatase, the temperature dependent shift of the oxygen ions in $SrTiO_3$ could be detected by a rotation of the magnetic axes of the charge compensated Fe^{3+} centres[58]. In rutile weak EPR spectra of Cr^{3+}, charge compensated by oxygen vacancies at second and third nearest neighbour sites[59] and of Co^{2+}, charge compensated at nearest neighbour sites[60], have been observed, however, not of Fe^{3+}. Again, at present no

definite answer can be given to the question why the charge compensation of Fe^{3+} in rutile is random and therefore not observed, while in anatase a strong EPR signal from $Fe^{3+} - V_o$ pairs is observed. An explanation may be that the attraction between an Fe^{3+} ion and a V_o centre is smaller in rutile than in anatase because of the higher dielectric constant of the first (114 vs. 48).

From the symmetry of the spectra II alone, it is possible that the oxygen vacancies are located one lattice distance farther in the same directions, 5.68 Å from the Fe^{3+} sites. In rutile, the zero field splitting of pure substitutional Cr^{3+} and of Cr^{3+} charge compensated at the third neighbour, which is 4.09 Å distant, differ by 20% [59]. It seems therefore unlikely that an oxygen vacancy 5.68 Å away from a Fe^{3+} ion could produce the large value of the crystal field at the Fe^{3+} site necessary to give the observed zero field splitting in anatase.

If the charge compensation of Fe^{3+} occurs only through V_o centres, then for every two Fe^{3+} ions one oxygen vacancy is required to obtain charge neutrality. If, in addition, the affinity between Fe^{3+} ions and V_o centres is sufficiently large to insure that all V_o centres are located at nearest neighbour sites of Fe^{3+}, the ratio of $Fe^{3+} - V_o$ pairs to pure substitutional Fe^{3+} would be 1 : 1. This compares to the experimental value $N_{II}/N_I = 0.3 \pm 0.1$ and implies that the charge compensation does not occur wholly through $Fe^{3+} - V_o$ pairs.

An interpretation of the temperature dependence of b_2^0 of spectrum I is a shift of the oxygen ions. This would imply that the axes of the crystal field of the charge compensated centre should shift with temperature. An increase of u should increase φ, the angle defining the magnetic axes of spectra II (for u = 0 one expects $\varphi = 0$). Lowering the temperature should therefore result in a decrease of φ. This decrease of φ with temperature was observed as shown in Table IV and Fig.16.

At room temperature one can empirically relate φ with the known value of α, the angle between the $Ti^{4+} - O^{2-}$ bond and the (100)-plane:

$$\varphi = 0.502\alpha.$$

If this relation remains valid also for other α, one obtains at 77 °K a value $\alpha_{77^o} = 12.26^o$. This means that the oxygen parameter u should decrease from 0.413 Å to 0.401 Å by lowering the temperature from 300 °K to 78°K.

There remains the question as to why the charge compensation occurs only at the four oxygen ions A-D and not at E or F of Fig.1. From symmetry one should expect that the magnetic axes of these latter paramagnetic centres coincide with the crystal axes and that the rhombic term b_2^2 be relatively small. It is possible that the weaker lines which could not be identified would account for these paramagnetic centres, but another explanation might be that a V_o centre at E or F is unstable and switches to one of the positions A-D.

6.3. Conclusions

The main results of the research of this thesis can be summarized as follows.

EPR measurements with natural single crystals of anatase show two types of spectra, generated by Fe^{3+} ions incorporated in the crystal structure of anatase at two different sites. At one site, designated I, the crystal field has axial symmetry and splits the ground state of Fe^{3+} only weakly, at the other site, designated II, the crystal field has orthorhombic or lower symmetry and splits the ground state of Fe^{3+} about 16 times more than at site I. For each Fe^{3+} at site II there are 3-5 Fe^{3+} at site I. The EPR spectra change markedly with temperature over the whole analysed range from 1 ^{o}K to 1230 ^{o}K. With increasing temperature the axial component of the crystal field at site I decreases (it is the largest temperature dependence of b_2^{o} of any EPR spectrum known to the author) and the crystal field at site II becomes more orthorhombic and the directions of its axes change slightly.

These EPR spectra are interpreted as due to Fe^{3+} ions regularly substituting Ti^{4+} (site I) and due to Fe^{3+} substituting Ti^{4+} with an oxygen vacancy (V_o-centre) at a nearest neighbour site (site II).

The temperature dependence of the two types of EPR spectra can be explained consistently by assuming that the

positions of the oxygen ions within the unit cell change with temperature. A definite confirmation of this proposed oxygen shift could be given with an X-ray crystal structure determination at high temperature.

The described EPR spectra of iron impurities in anatase are rather different from that obtained in rutile, in spite of the similarity of the structure of the two crystals.

Additional experimental investigations will be necessary to understand more fully the EPR spectrum of Fe in anatase and its difference from that in rutile. Of particular interest would be to understand the different defect structures of anatase and rutile.

EPR should be a useful tool to clarify these problems. The measurement of the pressure dependence of the EPR spectrum of Fe, the determination of the influence of reducing or oxidizing atmospheres on the concentration of the $Fe^{3+} - V_o$ centres and the analysis of EPR spectra of other transition element impurities, especially those of different valency, would yield useful information. However, to carry out these experiments, the technique of growing single crystals of anatase will have to be developed first.

BIBLIOGRAPHY

1. The historical development of the knowledge on polymorphism is described by M. Buerger and M. Bloom in "Crystal Polymorphism", Z. Krist. 96, 182 (1937). According to these authors, Klaproth was the first person to recognize a polymorphism in 1798 (calcite, aragonite)

2. A description of the early discoveries on these minerals is given by F. Barblan in "Untersuchungen zur Kristallchemie von Fe_2O_3 und TiO_2, sowie ihrer Alkaliverbindungen", Schweiz. Min. und Petro. Mit. 23, 295 (1943)

3. Simons, P. and Dachille, F., "The Structure of TiO_2II, a High Pressure Phase of TiO_2", Acta Crystallogr. 23, 334 (1967)

4. Czanderna, A., Clifford, A. and Honig, J., "Preparation of Highly Purified TiO_2 (anatase)", J. Am. Chem. Soc. 79, 5407 (1957)

5. Bach, H., "Zur Bildung von Brookit in dünnen TiO_2 Schichten", Naturwiss. 51, 10 (1964)

6. Gerritsen, H., "Paramagnetic Resonance of Transition Metal Ions in Rutile (TiO_2)", in Proceed. of 1st Intern. Conf. on Paramagnetic Res. (Edited by W. Low), Vol.1, p.3, Jerusalem (1962)

7. Low, W. and Offenbacher, E., "Electron Spin Resonance of Magnetic Ions in Complex Oxides", in Solid State Physics (Edited by F. Seitz and D. Turnbull), Vol.17, p. 135, Academic Press, New York (1965)

8. Low, W., "Electron Spin Resonance - A Tool in Mineralogy and Geology", Adv. in Electr. and Electron Phys. 24, 51 (1968)

9. Ghose, S., "Application of EPR in Silicate Minerals", in Short Lecture Notes on Resonance Spectroscopy in Mineralogy, Am. Geol. Institute (1968)

10. Horn, M. and Schwerdtfeger, C.F., "EPR of Substitutional and Charge Compensated Fe^{3+} in Anatase (TiO_2)", J. Phys. Chem. of Solids (to be published).

11. Bragg, L. and Claringbull, G., "The Crystalline State", Vol.IV, pp 107, Cornell University Press, New York (1966)

12. Cromer, D. and Herrington, K., "The Structures of Anatase and Rutile", J. Am. Chem. Soc. 77, 4708 (1955)

13. Pauling, L., "The Principles Determining the Structure of Complex Ionic Crystals", J. Am. Chem. Soc. 51, 1010 (1929)

14. Whittaker and Muntus, Geochem. Cosmochem. Acta 34, 945 (1970)

15. Navrotsky, A. and Kleppa, J., "Enthalpy of the Anatase Rutile Transformation", J. Am. Ceram. Soc. 50, 626 (1967)

16. Beard, W. and Foster, W., "High-Temperature Formation of Anatase", J. Am. Ceram. Soc. 50, 493 (1967)

17. Gmelins Handbuch der Anorganischen Chemie, Vol.41: Titan, Verlag Chemie, Weinheim (1951)

18. Czanderna, A., Rao, C. and Honig, J., "The Anatase-Rutile Transition", Trans. Faraday Soc. 54, 1069 (1958)

19. Rao, C., "Kinetics and Thermodynamics of the Crystal Structure Transformation of Spectroscopically Pure Anatase to Rutile", Can. J. Chem. 39, 498 (1961)

20. Yoganarasimhan, S. and Rao, C., "Mechanism of Crystal Structure Transformations", Trans. Faraday Soc. 58, 1579 (1962)

21. Shannon, R. and Pask, J., "Kinetics of the Anatase-Rutile Transformations", J. Am. Ceram. Soc. 48, 391 (1965)

22. Dachille, F., Simons, P. and Roy, R., "Pressure - Temperature Studies of Anatase, Brookite, Rutile and TiO_2II", Am. Min. 53, 1929 (1968)

23. Shannon, R. and Pask, J., "Topotaxy in the Anatase-Rutile Transformation", Am. Min. 49, 1707 (1964)

24. Pascal, ., "Nouveau Traité de Chimie Minérale", Vol. IX, p.96, Masson et Cie., Paris (1963)

25. Rao, K., Naidu, S. and Iyengar, L., "Thermal Expansion of Rutile and Anatase", J. Am. Ceram. Soc. 53, 124 (1970)

26. Schroeder, A., "Beiträge zur Kenntnis des Feinbaues des Brookits und des physikalischen Verhaltens sowie der Zustandsänderungen der drei natürlichen Titandioxyde", Z. f. Krist. 67, 485 (1928)

27. Errera, J. and Ketelaar, Hl, "Relations entre les Propriétés Optiques et Diélectriques et la Polarisation Ionique dans les Solids", J. Phys. et Radium 3, 239 (1932)

28. Gainon, D. and Lacroix, R., "EPR of Fe^{3+} Ion in Anatase", Proc. Phys. Soc. (London) 79, 658 (1962)

29. Barry, T., "ESR of Cr^{3+} in Anatase (TiO_2)", Solid State Comm. 4, 123 (1966)

30. Che, M., Gravelle, P. and Meriaudeau, P., "Etude par Resonance Paramagnétique Electronique d'un Bioxyde de Titane (Anatase) Contenant des Ions Antimoine", C.R. Acad. Sc. (Paris) 268C, 768 (1969)

31. Meriaudeau, P., Che, M. and Jorgensen, C., "Angular Overlap Treatment and ESR of Titanium (III) in Anatase", Chem. Phys. Letters 5, 131 (1970)

32. Hauser, C. and Cornaz, P., "Evidence by EPR of a Complex TiO^{3+} in the Crystal of TiO_2 Anatase", Chem. Phys. Letters 5, 226 (1970)

33. Cornaz, P., van Hooff, J., Pluijm, F. and Schuit, G., "Surface Coordination of Oxygen on Oxygen-Deficient TiO_2 and MoO_3 as Revealed by ESR Measurements", Dis. Faraday Soc. 41, 290 (1966)

34. Iyengar, R., Codell, M., Karra, J. and Turkevitch, J., "ESR Studies of the Surface Chemistry of Rutile", J. Am. Chem. Soc. 88, 5055 (1966)

35. Abragam, A. and Bleaney, B., "Electron Paramagnetic Resonance of Transition Ions", Clarendon Press, Oxford (1970)

36. Orbach, R., "Spin-Lattice Relaxation in Rare-Earth Salts", Proc. Roy. Soc. (London) 264A, 458 (1961)

37. Vinokurov, V., Zaripov, M. and Stepanov, V., "EPR of Mn^{2+} in Apatite", Sov. Phys.-Solid State 6, 866 (1964)

38. Vinokurov, V., Zaripov, M. and Stepanov, V., "EPR of Mn^{2+} in Diopside Crystals", Sov. Phys.- Solid State 6, 870 (1964)

39. Thyer, J., Quick, S. and Holuj, F., "ESR Spectrum of Fe^{3+} in Topaz", Can. J. of Phys. 45, 3597 (1967)

40. Horn, M. and Schwerdtfeger, C.F., "Reinterpretation and Temperature Dependence of EPR in TiO_2: Fe^{3+} (Anatase)", Solid State Comm. 8, 1741 (1970)

41. Bowers, K. and Owen, J., "Paramagnetic Resonance II", Rep. Progr. Phys. 18, p.321 (1955)

42. Serway, R., "Temperature-Dependent Spin Hamiltonian Parameters of Mn^{2+} in Trigonal Sites of $CaCO_3$, Phys. Rev. 3, 608 (1971)

43. Sharma, R., Das, T. and Orbach, R., "Zero-Field Splitting of S-State Ions. I. Point-Multipole Model", Phys. Rev. 149, 257 (1966)

44. Ja, Y., "EPR of Fe^{3+} and Mn^{2+} in Natural Single Crystals of Petalite $LiAlSi_4O_{10}$", Aust. J. Phys. 23, 299 (1970)

45. Sharma, R., "Temperature Variation of the Zero-Field Splitting in $CdCl_2$:Mn^{2+}", Phys. Rev. 2, 3316 (1970)

46. Walsh, W., Jeener, J. and Bloembergen, N., "Temperature-Dependent Crystal Field and Hyperfine Interactions", Phys. Rev. 139, A1338 (1965)

47. Horn, M. and Schwerdtfeger, C.F., "A Method to Obtain Directly the Angular Dependence of EPR Spectra in Single Crystal Studies", Rev. Scient. Inst. (to be published)

48. See for example: Ch. Poole "Electron Spin Resonance", Inter-Science Publisher, pp.367 (1967); or a more recent article: Goodrich, R. et al., Rev. Scient. Inst. 41, 245 (1970)

49. Giardino, D. and Petrakis, L., "High Temperature ESR Probe", Rev. Scient. Inst. 38, 1180 (1967)

50. Singer, L., Smith, W. and Wagoner, G., "Microwave Cavity for High Temperature ESR Measurements", Rev. Scient. Inst. 32, 213 (1961)

51. Troup, G. and Hutton, D., "Paramagnetic Resonance of Fe^{3+} in Kyanite", Brit. J. Appl. Phys. 15, 1493 (1964)

52. Aasa, R., "Powder Line Shapes in the EPR Spectra of High Spin Ferric Complexes", J. Chem. Phys. 52, 3919 (1970)

53. Byfleet, C., Chong, D., Hebden, J. and McDowell, J., J. of Magn. Res. 2, 69 (1970)

54. Holuj, F., "The Spin Hamiltonian and Intensities of the ESR Spectra Originating from Large Zero-Field Effects on ^6S States", Can. J. Phys. 44, 503 (1966)

55. Lichtenberger, G. and Addison, J.R., "F-and X-band Spectroscopy on Fe^{3+} in Rutile", Phys. Rev. 184, 381 (1969)

56. Carter, D. and Okaya, A., "EPR of Fe^{3+} in TiO_2 (Rutile)", Phys. Rev. 118, 1485 (1960)

57. Kirkpatrick, E., Müller, K. and Rubins, R., "Strong Axial EPR Spectrum of Fe^{3+} in $SrTiO_3$ Due to Nearest-Neighbour Charge Compensation", Phys. Rev. 235, A86 (1964)

58. Müller, K. and Berlinger, W., "Static Critical Exponents at Structural Phase Transitions", Phys. Rev. Letters 26, 13 (1971) and references quoted therein.

59. Ikebe, M., Miyako, Y. and Date, M., "ESR of Cr^{3+} Ions Coupled with Oxygen Vacancies in Rutile", J. Phys. Soc. Japan 26, 43 (1969)

60. Miyako, Y., "ESR of Co^{2+} Ions Combined with Defects in Rutile", Phys. Letters 24A, 635 (1967)

APPENDIX A

Matrix of the Spin Hamiltonian (8) for S = 5/2 and the Magnetic Field H along one of the Coordinate Axes

Table V Matrix of the Spin Hamiltonian (8) for S = 5/2 and H // z

$h = g \beta H$

	$\lvert +5/2 \rangle$	$\lvert +1/2 \rangle$	$\lvert -3/2 \rangle$	$\lvert -5/2 \rangle$	$\lvert -1/2 \rangle$	$\lvert +3/2 \rangle$
$\langle +5/2 \rvert$	$\frac{5}{2}h + \frac{10}{3}b_2^0 + b_4^0$	$\frac{\sqrt{10}}{3}b_2^2 + \frac{3\sqrt{10}}{20}b_4^2$	$\frac{1}{\sqrt{5}}b_4^4$			
$\langle +1/2 \rvert$	$\frac{\sqrt{10}}{3}b_2^2 + \frac{3\sqrt{10}}{20}b_4^2$	$\frac{1}{2}h - \frac{8}{3}b_2^0 + 2b_4^0$	$\sqrt{2}b_2^2 - \frac{\sqrt{2}}{4}b_4^2$		0	
$\langle -3/2 \rvert$	$\frac{1}{\sqrt{5}}b_4^4$	$\sqrt{2}b_2^2 - \frac{\sqrt{2}}{4}b_4^2$	$-\frac{3}{2}h - \frac{2}{3}b_2^0 - 3b_4^0$			
$\langle -5/2 \rvert$				$-\frac{5}{2}h + \frac{10}{3}b_2^0 + b_4^0$	$\frac{\sqrt{10}}{3}b_2^2 + \frac{3\sqrt{10}}{20}b_4^2$	$\frac{1}{\sqrt{5}}b_4^4$
$\langle -1/2 \rvert$		0		$\frac{\sqrt{10}}{3}b_2^2 + \frac{3\sqrt{10}}{20}b_4^2$	$-\frac{1}{2}h - \frac{8}{3}b_2^0 + 2b_4^0$	$\sqrt{2}b_2^2 - \frac{\sqrt{2}}{4}b_4^2$
$\langle +3/2 \rvert$				$\frac{1}{\sqrt{5}}b_4^4$	$\sqrt{2}b_2^2 - \frac{\sqrt{2}}{4}b_4^2$	$\frac{3}{2}h - \frac{2}{3}b_2^0 - 3b_4^0$

Table VI Expressions to be Inserted in Place of b_n^m in Table V for the Cases when H is along the x and y Axis

This Table is given by Thyer et al.[39]. Some numerical errors are corrected.

	H // x	H // y
b_2^0	$-(b_2^0 - b_2^2)/2$	$-(b_2^0 + b_2^2)/2$
b_2^2	$(3\,b_2^0 + b_2^2)/2$	$(3\,b_2^0 - b_2^2)/2$
b_4^0	$(3\,b_4^0 - b_4^2 + b_4^4)/8$	$(3\,b_4^0 + b_4^2 + b_4^4)/8$
b_4^2	$-(5\,b_4^0 - b_4^2 - b_4^4)/2$	$-(5\,b_4^0 + b_4^2 - b_4^4)/2$
b_4^4	$(35\,b_4^0 + 7\,b_4^2 + b_4^4)/8$	$(35\,b_4^0 - 7\,b_4^2 + b_4^4)/8$

APPENDIX B

Approximate Calculation of b_2^0 and b_2^2 of Spectrum II

The main features of the EPR spectrum of Fe^{3+} ($S = 5/2$) in a strong crystal field can be described with the spin Hamiltonian

$$\mathcal{H} = 2\beta \cdot \vec{H} \cdot \vec{S} + D S_z^2 + E (S_x^2 - S_y^2) \qquad (19)$$

This implies that two parameters, D ($= b_2^0$) and E ($= b_2^2/3$), together with the directions of the magnetic axes, are sufficient to characterize the spectrum. These parameters can be estimated with the help of graphs given by Troup et al.[51] and Aasa[52], if the transition fields along the magnetic axes are measured.

Troup et al.[51] calculate the effective g values of the transitions within the three Kramer doublets of the ground state of Fe^{3+} as a function of E/D for $D \gg h\nu$.

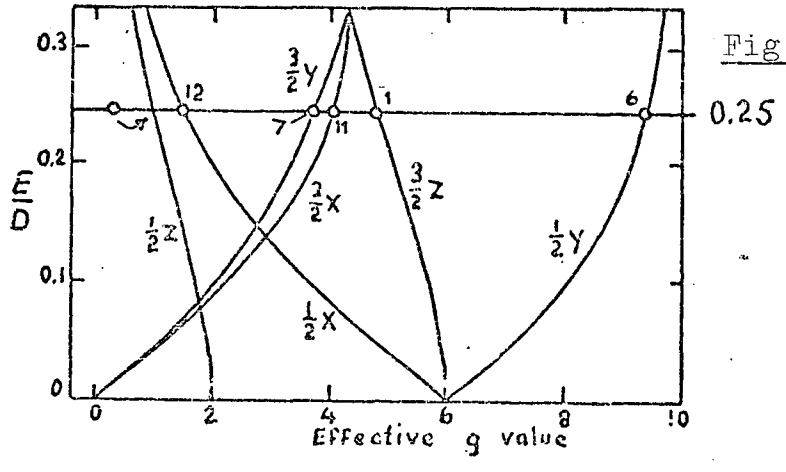

Fig. 18 Effective g values at low field for transitions within the two lower Kramer doublets of the ground state of Fe^{3+} (Ref. 51)

$h\nu$ is the microwave photon energy. Fig.3 of Troup et al.[51] is partially given here as Fig.18. $\frac{1}{2}$ z means a transition within the doublet $|\pm 1/2\rangle$ and the magnetic field H//z, etc. Transitions within the doublet $|\pm 5/2\rangle$ are not shown in Fig.18. The experimentally observed transitions at X-band of spectrum II in anatase are indicated and numbered as in Fig.13. One deduces from the graph $E/D = 0.25 \pm 0.02$.

Aasa[52] calculates for $S = 5/2$ the transition fields B as a function of D, using E/D as a parameter. D and B are measured in units of $h\nu$. In Fig.19 are reproduced those parts of Aasas figures 1 and 7 which correspond to $E/D = 0.25$. The transitions for B parallel to the coordinate axes are shown in the upper part of Fig.19 for the lowest Kramer doublet, in the lower part of the figure for the intermediate Kramer doublet (Aasa labels the energy levels according to their relative magnitude, $3 \leftrightarrow 4$ means therefore a transition within the $|\pm 3/2\rangle$ doublet). The observed transitions of spectrum II in anatase are again indicated and labeled as in Fig.13. From these graphs a value of $h\nu/D = 0.65 \pm 0.05$ is deduced. Together with $\nu = 9.19$ GHz, this results in $|D| = 14.2 \pm 1$ GHz.

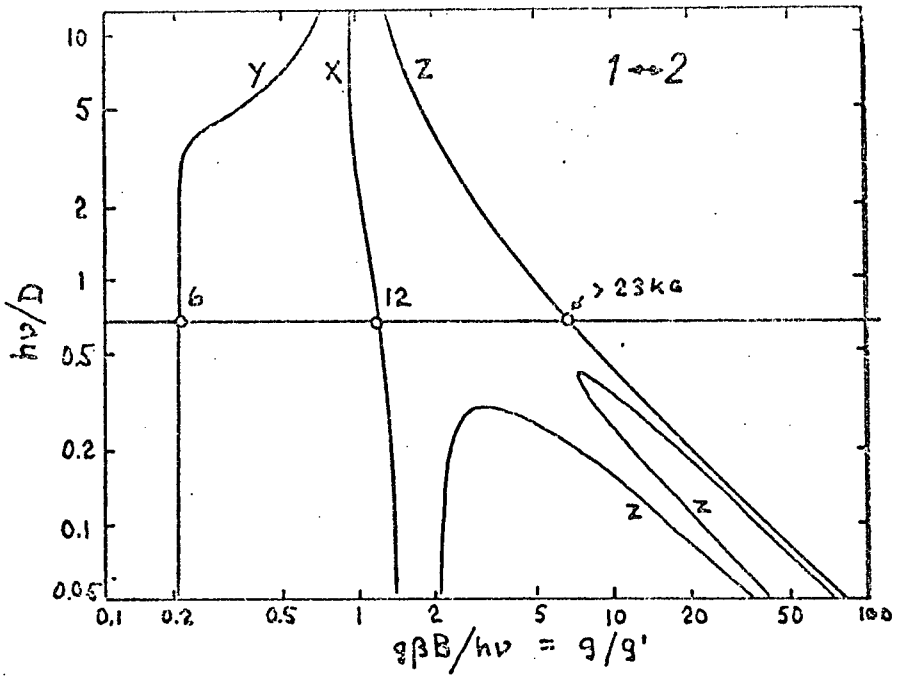

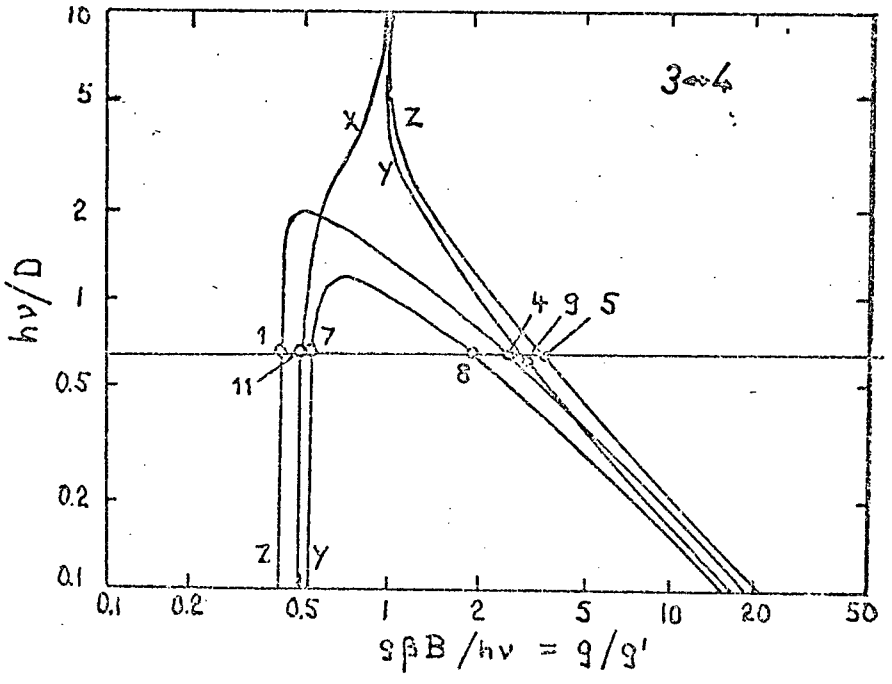

Fig.19 Positions of the EPR transitions within the two lower Kramer doublets of Fe^{3+} for E/D = 0.25 (Ref.52)

APPENDIX C

Calculation of Spin Hamiltonian Parameters with a Linearized Least Mean Square Fit

As discussed in section 5.4., the observed EPR transition fields H_k^{exp} , k = 1, ..., 13, of spectrum II in anatase are fit to the truncated Hamiltonian (19) with a trial and error method using a computer programme given by Hebden et al.[53]. The best fit, at room temperature, is obtained with

$$b_2^0 = 0.501 \quad cm^{-1}$$

$$b_2^2 = 0.375 \quad cm^{-1}$$

and gives calculated transition fields H_k^o .

The above values of b_2^0 and b_2^2, together with $b_4^0 = b_4^2 = b_4^4 = 0$, are used as approximate values $(b_n^m)_o$ in a Newton-Raphson interpolation calculation to determine the constants of the spin Hamiltonian (8).

The parameters $(b_n^m)_o$ are individually changed by a small amount δb_n^m and the new transition fields, which differ by δh_k from H_k^o, are calculated by diagonalizing with a computer programme the energy matrix given in table V. H_k^{cal} is now defined by

$$H_k^{cal} = H_k^o + \sum_{n,m} \Delta b_n^m \cdot \frac{\delta h_k}{\delta b_n^m} \qquad (20)$$

This represents a system of k linear equations in the unknowns Δb_n^m. The best values of Δb_n^m are determined by minimizing

$$\sum_k (H_k^{exp} - H_k^{cal})^2 \qquad (21)$$

The results, $b_n^m = (b_n^m)_o + \Delta b_n^m$ are included in Table II and discussed in section 5.4.